OPEN ACCESS
IOP Publishing
Journal of Physics D: Applied Physics
J. Phys. D: Appl. Phys. **47** (2014) 374008 (22pp)
doi:10.1088/0022-3727/47/37/374008

Terahertz imaging using quantum cascade lasers—a review of systems and applications

P Dean[1], A Valavanis[1], J Keeley[1], K Bertling[2], Y L Lim[2], R Alhathlool[1], A D Burnett[1], L H Li[1], S P Khanna[1], D Indjin[1], T Taimre[3], A D Rakić[2], E H Linfield[1] and A G Davies[1]

[1] School of Electronic and Electrical Engineering, University of Leeds, Leeds, LS2 9JT, UK
[2] School of Information Technology and Electrical Engineering, The University of Queensland, St Lucia, QLD 4072, Australia
[3] School of Mathematics and Physics, The University of Queensland, St Lucia, QLD 4072, Australia

E-mail: p.dean@leeds.ac.uk

Received 21 May 2014, revised 4 July 2014
Accepted for publication 11 July 2014
Published 28 August 2014

Abstract

The terahertz (THz) frequency quantum cascade laser (QCL) is a compact source of THz radiation offering high power, high spectral purity and moderate tunability. As such, these sources are particularly suited to the application of THz frequency imaging across a range of disciplines, and have motivated significant research interest in this area over the past decade. In this paper we review the technological approaches to THz QCL-based imaging and the key advancements within this field. We discuss in detail a number of imaging approaches targeted to application areas including multiple-frequency transmission and diffuse reflection imaging for the spectral mapping of targets; as well as coherent approaches based on the self-mixing phenomenon in THz QCLs for long-range imaging, three-dimensional imaging, materials analysis, and high-resolution inverse synthetic aperture radar imaging.

Keywords: imaging, quantum cascade lasers, terahertz

(Some figures may appear in colour only in the online journal)

1. Introduction

The field of terahertz (THz) science and technology has witnessed remarkable growth over the past decades, in part due to the considerable advances made in technologies for generation and detection of THz frequency radiation [1, 2]. Much of this progress has been motivated by the wide range of potential applications of THz waves, of which many are particularly suited to imaging technologies [3] within diverse areas such as biomedicine, security controls, industrial inspection, non-destructive analysis and spectroscopic mapping of illicit materials [2, 4, 5].

The specific appeal of THz radiation for imaging applications has been acknowledged for several decades [6], and there has been significant interest in this technology following the first practical demonstrations of THz imaging [7, 8]. This interest has stemmed primarily from the attractive properties of THz radiation, which bear similarities with each of the neighbouring infrared and microwave spectral regions, yet are unique in combination to this part of the spectrum. Foremost, THz radiation is able to penetrate many dry, non-polar and non-metallic materials that are typically opaque at visible/infrared frequencies. These include plastics, paper/cardboard, ceramics, wood and fabrics (although only below ∼1 THz in the latter case). It is this penetrative ability, coupled with the promise of sub-millimetre diffraction-limited imaging resolution, that has driven interest in imaging applications within the security sector as well as

for non-destructive inspection and quality control [4, 9, 10]. One notable example of this has been for the characterization of thickness and uniformity of the coating of pharmaceutical tablets [9, 11]. The second important property of THz waves is their ability to excite vibrational modes in a range of organic and inorganic materials. This characteristic, which is not exhibited by millimetre waves, enables (concealed) samples to be discriminated based on their chemical composition as well as their crystalline structure [11, 12]. This has motivated the application of THz imaging to the identification and two-dimensional mapping of chemicals [13–15] including illicit drugs and explosives [16–18]. Further properties of THz radiation also lend themselves to the study of biological samples and biomedical imaging applications. Owing to the relatively low photon energies in this region of the spectrum, THz radiation is non-ionizing. Photons of this energy range are also known to excite intermolecular interactions in liquid water, which exhibits a strong and broad absorption around 5.4 THz that extends to lower frequencies [19]. As such, the degree of THz absorption can be used to distinguish between muscle and fat as well as benign and malignant tissues [20, 21]. Such imaging approaches also benefit from reduced scattering within biological tissue owing to the longer wavelength in comparison to visible/near-infrared radiation.

Until recently, the majority of THz imaging systems reported have been based on the principles of time-domain spectroscopy (TDS) [12] in which the sample is raster-scanned through the focused beam and the THz field sampled optically in the time domain at each pixel [3, 22]. Through this approach both the amplitude and phase spectrum of the reflected/transmitted THz field can be mapped spatially across the sample over bandwidths as large as 100 THz [23], in principle. However, broadband THz pulse imaging (TPI) systems of this kind typically suffer from limited spectral resolution no better than ∼5 GHz (and worse in high-bandwidth systems) as well as usable dynamic range only below ∼3 THz. In addition, TPI systems are restricted to low THz powers, typically ∼ μW for the optically pumped photoconductive emitters commonly employed. Other drawbacks include slow acquisition due to the requirement for mechanical scanning of the optical delay at each pixel, as well as the reliance on bulky and expensive ultrafast laser sources for the generation and detection of THz radiation. In addition to time-domain approaches, a range of narrowband continuous-wave (cw) sources have been applied to THz imaging in the frequency domain. These include THz parametric oscillators [15, 16], backward-wave oscillators [24], multiplied Gunn emitters [25] and cw photomixers [26, 27]. Such systems offer the advantage of compactness, high spectral purity and potentially faster acquisition rates, although these sources also typically suffer from low powers or are restricted to sub-THz operating frequencies.

In recent years, however, the quantum cascade laser (QCL) [28, 29] has emerged as a compact, high power, spectrally pure source for the THz frequency range. The gain media in QCLs consist of hundreds of thin layers of alternating semiconductor materials (typically GaAs and AlGaAs, grown using molecular-beam epitaxy), in which electrons are confined into discrete energy subbands. These layers form periodic modules, and when placed in an external electric field, the electrons 'cascade' from period-to-period, emitting a low-energy photon at each step. As such, the photon energy is not determined by the bandgap of the material, but may be chosen over a wide range of values by engineering the widths of the semiconductor layers. Following remarkable development over the past decade, QCL devices have now been demonstrated with emission frequencies throughout the range 1.2–5.2 THz [30, 31]. Operating temperatures have reached up to 199.5 K when operated in pulsed mode [32], and 129 K in cw operation [33], which is preferred for coherent detection schemes. Peak powers have recently been reported to exceed 1 W in pulsed mode [34], whereas under cw operation output powers greater than 100 mW have been achieved [35]. Devices have recently been shown to exhibit sub-kilohertz quantum-noise-limited linewidths [36] and also offer potential for tunability [37]. As such, these sources offer tremendous benefits in terms of imaging capability compared to the broadband sources commonly used in TPI—namely: high source powers exceeding those of optically pumped and thermal sources by several orders of magnitude; high spectral purity suitable for coherent, narrowband imaging schemes [38, 39]; access to frequencies greater than 3 THz where many materials exhibit spectral absorption features [40]; and the potential for the development of compact imaging systems that do not rely on bulky, ultrafast laser sources [41–43]. These appealing characteristics have not only motivated significant research interest over the past decade but also offer great potential for the further advancement of THz imaging technologies. In this paper, we review the technological approaches to THz QCL-based imaging, with particular emphasis on the benefits offered by these sources in terms of high dynamic range, spatial resolution, fast acquisition and spectral specificity. After reviewing the key advancements within this field, in sections 3–6 we focus on a number of imaging approaches particularly suited to potential applications, namely: multiple-frequency transmission imaging for spectroscopic mapping of materials; diffuse reflection imaging (DRI) for the spectral analysis of powders; and coherent imaging based on the self-mixing (SM) phenomenon in THz QCLs, for long-range imaging, three-dimensional imaging, materials analysis and high-resolution inverse synthetic aperture radar (ISAR) imaging.

2. Advancements in THz QCL-based imaging

2.1. Incoherent imaging with high dynamic range

Perhaps the most apparent benefit offered by THz QCLs is their high emission power, which is typically several orders of magnitude greater than the power available from the optically pumped broadband sources usually employed in TPI. In terms of imaging system capabilities this high source power translates directly to high dynamic range—or equivalently the degree of attenuation by the target that can be tolerated by the detection scheme. Indeed, for a given noise-equivalent power (NEP) these quantities scale linearly with the source power.

As for many systems reported to date, the early demonstrations of imaging using THz QCL sources [44–46] adopted incoherent thermal detection, thereby foregoing the advantages of coherent detection offered by TPI approaches. These studies nevertheless confirmed that a high dynamic range can be achieved with cryogenically cooled bolometric detection. For example, Kim *et al* reported a dynamic range of 33 dB with a peak THz power of 4 mW, despite the QCL being driven with low duty cycle [46]. This capability made possible the study of highly attenuating samples including rat brain sections [44] and metastatic liver cancer [46] in two early demonstrations. Optimized experimental arrangements employing sources with higher time-averaged powers in conjunction with cryogenically cooled bolometric detection have since achieved a dynamic range ∼49 dB for a lock-in time constant of 10 ms, and up to 64 dB for longer acquisition times [40]. Recently, the use of nanowire field-effect transistors has led to a signal-to-noise ratio (SNR) approaching 80 dB Hz^{-1} in an imaging system employing a 2.8 THz QCL emitting 2 mW in cw [47]. In respect of these specifications it is of particular significance that THz QCLs provide access to the spectral region above 2 THz, where TPI systems typically offer very limited dynamic range owing to the drastically reduced source power at these frequencies. It should also be noted that further improvements in dynamic range can be accomplished by combining the high power of THz QCLs with the benefits of coherent detection. For example, a dynamic range of 60 dB has been reported using a pseudo-heterodyne technique based on the mixing between adjacent longitudinal cavity modes on a Schottky diode, with a time constant as low as 10 μs, in principle [48]. Coherent imaging approaches will be discussed further in sections 5 and 6.

2.2. Imaging with high spatial resolution

The higher operating frequencies of THz QCLs compared to TPI sources and electronic frequency-domain sources enable high transverse resolutions with minimum feature sizes smaller than 250 μm [46, 47, 49, 50]. For context, the diffraction-limited beam waist expected for a TEM_{00} (Gaussian) mode focused by a lens with f-number $f/1$, at a wavelength $\lambda = 100\,\mu$m (∼3 THz), is calculated to be $w_0 = 2\lambda f/\pi = 64\,\mu$m. It is perhaps not surprising, though, that diffraction-limited resolution is seldom realized in experimental systems due to the irregular beam profiles exhibited by THz QCLs. Metal–metal (MM) waveguides offer high modal confinement, enabling the realization of devices with high operating temperatures and low threshold current densities [51]. However, as a result of the sub-wavelength aperture in this waveguide design (typically ∼10 μm thick), the output beam becomes strongly diffracted. The associated beam patterns [52] are extremely poor, limiting the usefulness of this type of waveguide for many potential applications of THz QCLs. The alternative and more common approach is to employ a semi-insulating surface plasmon (SP) waveguide [28]. SP waveguides typically provide lower waveguide losses than MM waveguides as a result of the waveguide mode partially overlapping with the undoped substrate. More significant, though, is the superior beam quality and reduced beam divergence [53, 54] that results from this approach. QCL-based imaging systems reported to date have therefore exclusively employed SP waveguides. Nevertheless, the beam profile of such devices is still not ideal. Far-field profiles have been shown to comprise dual emission lobes originating from beam diffraction from both the substrate and waveguide ridge [41, 42, 55]. The emission profile is also typically characterized by extensive ring-like interference fringes [54, 56] that can be understood using a wire laser model that treats the device as a longitudinally distributed source [57].

In order to address these considerations and realize better optimized image resolution, hollow dielectric waveguides have been employed to efficiently couple the QCL emission to the free-space TEM_{00} (Gaussian) mode [58, 59]. An alternative approach is through spatial filtering of the QCL beam, which has been successfully employed for the development of a transmission-mode THz confocal microscope based on a QCL source emitting at 2.9 THz [50]. In this scheme the QCL beam was first spatially filtered using a 200 μm (∼2λ) aperture placed in the common focal plane of a pair of matched (NA∼0.45) lenses. Figures 1(*a*) and (*b*) demonstrate the resulting improvement in beam quality, measured in a plane close to the cryostat window and also close to the aperture. For the purpose of rejecting out-of-focus radiation, this spatially filtered beam was then focused through the sample under test, followed by a 300 μm confocal aperture. This aperture was found to enhance image contrast whilst also reducing the depth of field, and the complete system yielded an impressive transverse resolution better than 70 μm with an axial resolution of ∼400 μm. Figures 1(*c*)–(*e*) show THz images of a fresh green leaf containing minute veins, which amply demonstrate the high resolution attainable through this spatially filtered confocal arrangement.

2.3. Imaging with fast acquisition rates

The majority of THz QCL-based imaging approaches acquire images by raster-scanning the sample through the focused THz beam, whilst recording the detector response on a 'pixel-by-pixel' basis. Whilst experimentally convenient, this approach is not applicable to many real-world applications and also results in slow acquisition. Many factors influence the image acquisition rate including the source power, the NEP of the detection scheme (which together dictate the degree of signal integration required for a satisfactory noise figure in the images), and the response time of the detection. In this regard it is worth noting that imaging systems commonly employ incoherent thermal detection using Golay cells [42, 60], cryogenically cooled bolometers [40, 44, 46, 50, 61] or pyroelectric sensors [61], which are typically slow (response times ∼1–100 ms) owing to the relatively long time constants of thermal processes. Image acquisition rates can therefore range from several seconds per pixel to tens of pixels per second (pps) in these systems, with total practical image acquisition times ranging from several minutes to hours for larger images. For optimized systems in which faster acquisition is feasible, imaging times can still be severely limited due to software/hardware data processing rates [48]

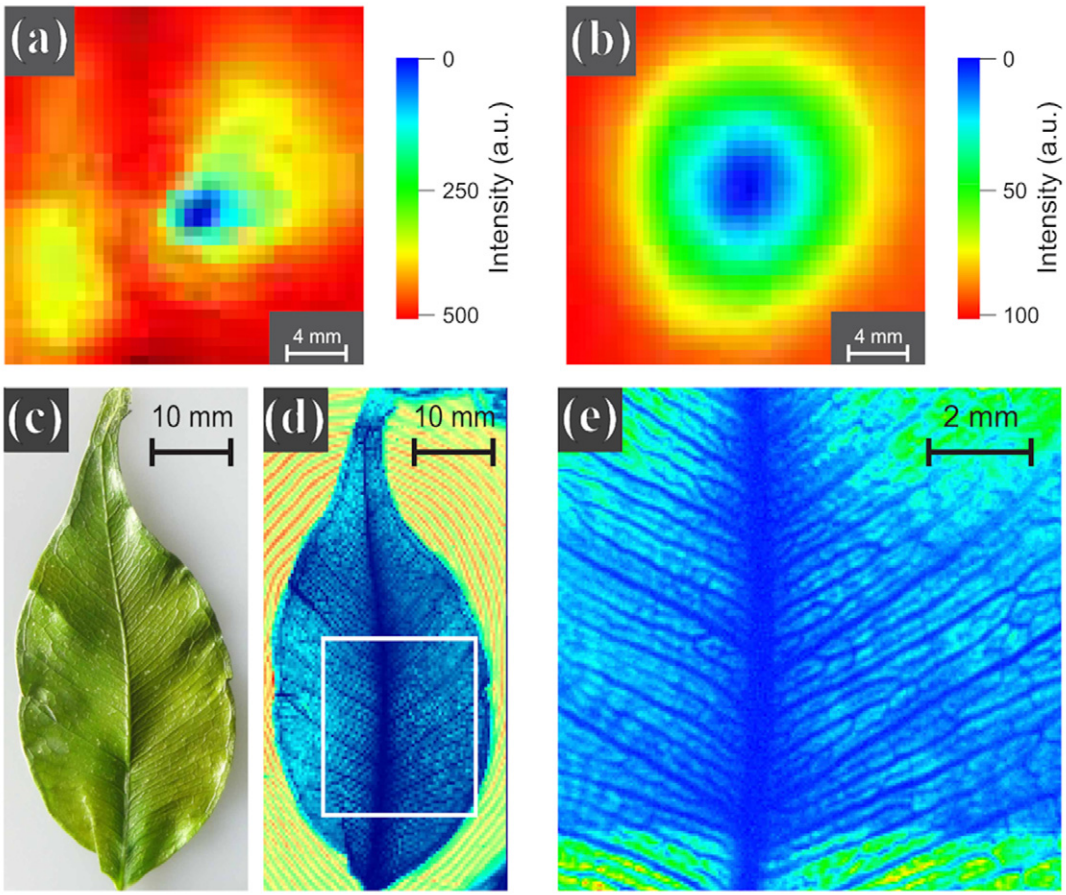

Figure 1. Far-field profile of a 2.9 THz QCL measured at (*a*) the QCL output and (*b*) after spatial filtering using a 200 μm aperture. (*c*) Photograph of a fresh leaf and corresponding high-resolution THz images acquired with a (*d*) 200 μm step size and (*e*) 50 μm step size. (Adapted with permission from [50], Copyright 2012 The Optical Society).

and delays incurred by mechanical scanning of the sample [49, 61]. Limitations such as those described have recently been overcome in an impressive demonstration employing a fast scanning mirror in conjunction with a fast Ge : Ga photoconductive detector [62]. In this system (see figure 2(*a*)), the collimated beam from a 2.5 THz QCL was deflected onto a high density polyethylene (HDPE) lens using a flat scanning mirror, the angle of which could be controlled to a resolution of 2 μrad. This varying deflection angle translated to a transverse displacement of the beam waist in the object plane, which could be controlled to within 1 μm over an object plane measuring 36 mm by 40 mm. The beam transmitted through the sample was then focused to the detector. Owing to the fast scanning capability of the deflecting mirror, the short response time of the detector, and the fast (500 kHz) digital acquisition, this system was capable of acquiring a two-dimensional (2D) image comprising 4550 pixels within just 1.1 s (~4140 pps). Despite the moderate source power (~300 μW) the dynamic range of this system could reach 28 dB, with a spatial resolution of 0.5 mm. The fast acquisition rates realized have also enabled fast three-dimensional (3D) imaging by computer tomography (CT), achieved by obtaining successive 2D projection images taken from different illumination angles using a rotation stage synchronized with the 2D beam scanning. Figures 2(*b*) and (*c*) show a photograph and corresponding CT image of a polyethylene bag filled with TPX pellets with diameter ~4 mm, obtained using this system. For the 60 projection angles acquired for 3D imaging by CT, an imaging time of 87 s was required, corresponding to approximately 3100 pps. For comparison, an alternative CT system [60, 63] employing traditional raster-scanning of the sample and a Golay cell detector reported an acquisition time of 15 min per 2D projection comprising up to 289 pixels sampled at each of 18 projection angles. This corresponds to an acquisition rate of only ~6 pps, which highlights the huge improvement that can be realized through employing a beam-steering approach in an optimized imaging system. It is also worth noting that, in addition to enabling fast 2D and 3D sample reconstruction at THz frequencies, this fast scanning system can accurately and quickly direct high THz powers to a specific spatial location. This capability opens up the possibility of targeted spectroscopic analysis of regions of interest within a target. A similar approach has successfully been employed for sub-THz detection of powders within envelopes, and their subsequent THz spectroscopic analysis, as part of a mail-scanning system employing x-ray, sub-THz and THz spectral bands [64].

For many of the potential applications of THz imaging, real-time imaging rates (~25 frames per second (fps)) would be highly desirable. Not only does such capability enable moving targets to be captured without image degradation due

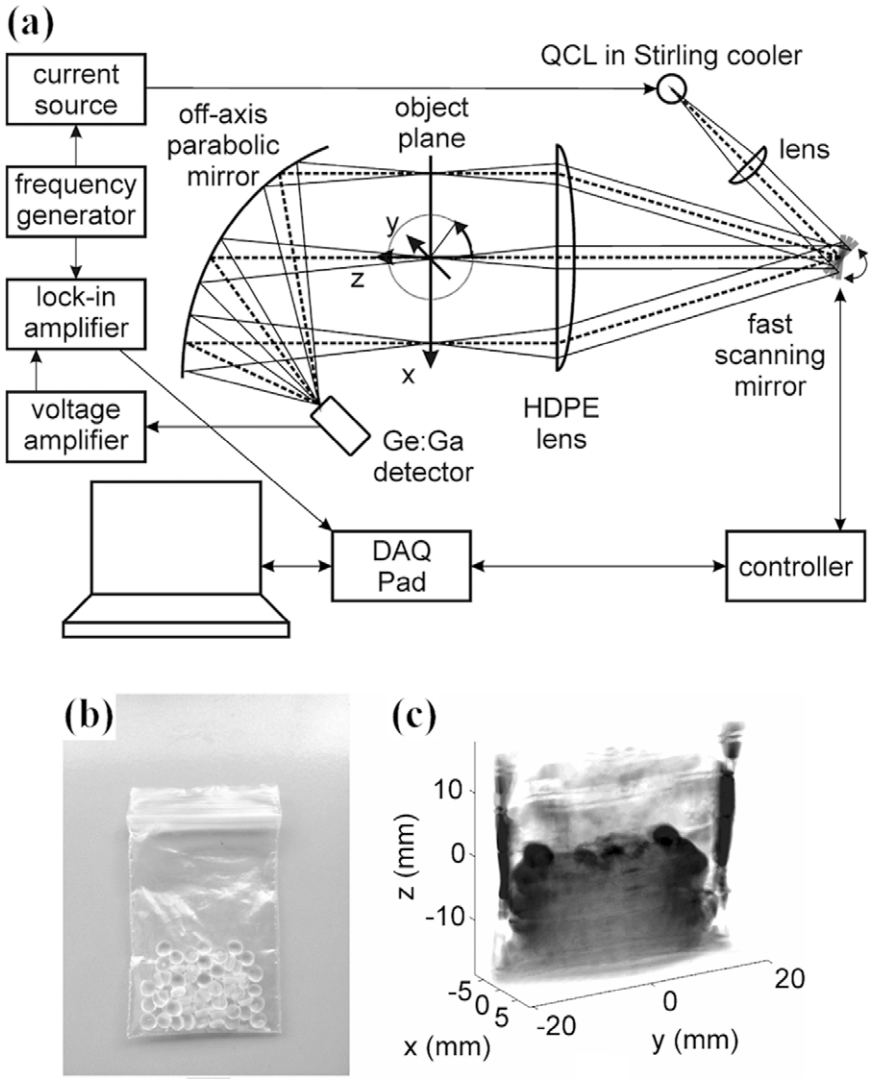

Figure 2. (*a*) Experimental apparatus for fast THz imaging and tomography by steering of the THz beam. (*b*) Photograph and (*c*) CT image of a polyethylene bag filled with TPX pellets with diameter ∼4 mm, acquired at a frequency of 2.5 THz. (Adapted with permission from [62], Copyright 2013 IEEE).

to motion artefacts, it can also improve the perceived image clarity by exploiting the integration abilities of the eye and pattern recognition of the brain. The most straightforward means of achieving real-time imaging is through the use of multi-pixel 2D detector arrays. At THz frequencies this most commonly requires the use of microbolometer or pyroelectric arrays, although approaches for up-converting the THz field to visible/near-infrared frequencies and thereby enabling the use of traditional CCD technology have been reported, albeit with slower acquisition rates [65]. Crucial to such approaches, though, is the capacity to illuminate the 2D array with sufficient power density to achieve a reasonable noise figure within each pixel. In this respect the high average powers of THz QCLs offer a tremendous advantage over common TPI sources and sub-terahertz electronic sources. This has enabled real-time imaging to be reported through the range 2.8–4.9 THz [66–68]. The first of these demonstrations employed a 320 × 240 element room-temperature vanadium oxide microbolometer focal plane array (FPA). Although designed for the 7.5–14 μm band, the elements of this FPA exhibit absorption in the THz range. As such the THz images were affected by the infrared background, which was removed using a frame subtraction technique. The source used was a 4.3 THz QCL based on the resonant-phonon depopulation scheme emitting 50 mW peak power when operated at a temperature of 33 K in a closed-cycle pulse-tube cryorefrigerator. The QCL was modulated synchronously with the 60 fps sampling rate of the FPA enabling acquisition of frames both under THz illumination and after the THz signal had decayed sufficiently. By subtracting the latter from the former, adequate suppression of the common-mode infrared background was accomplished with the additional benefit of reducing $1/f$ noise. Through this sampling sequence the imaging frame rate was subsequently reduced to 20 fps, but still suitable for real-time video imaging. At this imaging rate, a NEP of $\sim$320 pWHz$^{-0.5}$ was reported for the detector, yielding an SNR$\sim$340 (not accounting for pulse-to-pulse instability). It is anticipated that these figures could be improved through the use of higher power sources and by optimization of the microbolometer absorber for THz frequencies. In this first demonstration of real-time imaging,

three transmission-mode videos were presented of (1) pencil writing through an envelope, (2) a plastic mechanical pencil and (3) a metal screw embedded in polystyrene. Other reports similarly employing vanadium oxide FPAs [68] have presented videos of a metallic blade obscured by visibly opaque plastic tape. One drawback of these full-field 2D imaging approaches worthy of mention, though, is the presence of strong fringe patterns in the THz images arising from diffraction, etalon and interference effects [68, 69]. Nevertheless, the prospect of quantum-well infrared photodetector arrays [70] and nanowire field-effect transistor arrays [47] promise advancements in video-rate imaging approaches.

2.4. Imaging over extended distances

The ability to tailor the emission frequency of THz QCLs represents another feature of these sources that improves their applicability across a range of application areas. Several methods of spectral control exist, including: quantum engineering of the active region heterostructure [71]; exploiting the strong Stark shift of the transition energy with applied electric field in active regions with diagonal transitions [72]; or selecting a specific emission frequency within the gain bandwidth of the active region (which can exceed 10% of the central emission wavelength [73–75]) through the use of distributed-feedback resonators [76–78] or frequency tuning mechanisms [37]. A further consideration relevant to the spectral selectivity of THz QCLs is their linewidth. Studies have recently shown that THz QCLs exhibit sub-kHz quantum noise-limited linewidths [36, 79]. However, owing to the presence of thermally and electrically induced noise, such sources are susceptible to frequency drifts and line broadening. As such, without active frequency stabilization, attainable instantaneous linewidths are limited to the range greater than 10 kHz in practice [55, 80, 81], although the emission frequency can drift more than 10 MHz over longer integration times [80–82].

In respect of imaging systems, this degree of frequency selectability, coupled with the high power spectral density arising from the narrow linewidth, is suitable for targeting transmission windows in the atmospheric absorption spectrum and thereby permitting imaging over extended ranges. Indeed, long-range imaging at THz frequencies is known to be challenging owing to the presence of atmospheric water vapour that can strongly absorb THz radiation where typical attenuation factors are in the range between ∼0.5 and ∼10 dB m^{-1}, sometimes exceeding the latter [83]. Simple analysis [67] has led to the important conclusion that, owing to the exponential rate of attenuation dictated by the Beer–Lambert law, the radiation frequency is far more important than source power in terms of delivering power to a remote target or detector. For example, for an optical path length of 25 m, the power delivered decreases by more than one order of magnitude for an increase in atmospheric loss of only 0.5 dB m^{-1}, and the loss can change by more than this amount over a frequency range on the order of GHz. Conversely, power delivered to the target scales only linearly with source power.

Bearing these considerations in mind, demonstrations of coherent imaging over a round-trip distance >20 m [84] (see section 6.1) and incoherent real-time imaging over >25 m [67] using QCL sources emitting within atmospheric windows at ∼2.6 THz and ∼4.9 THz, respectively, have been reported. In the latter case this emission frequency was achieved through a combination of quantum engineering of the heterostructure and by exploiting the Stark effect; by using a shorter lasing cavity (∼2 mm) to increase the effective mirror losses, a higher applied field at lasing threshold was required, leading to the gain becoming clamped at an increased emission frequency of 4.9 THz. At this frequency the atmospheric loss was estimated to be ∼0.5 dB m^{-1}. The QCL device used in this demonstration was based on a resonant-phonon depopulation scheme, and emitted 17 mW peak power (∼4.6 mW average power) at the operating temperature of 30 K. Radiation from the laser was collimated using an off-axis $f/1$ parabolic reflector and folded through an extended distance (24.5 m) using four planar mirrors. A spherical mirror of diameter 15 cm was then used to image the object plane on a microbolometer FPA (see section 2.3). Two imaging configurations were used. For low-resolution (estimated to be ∼3 mm) imaging the object plane was located 2 m in front of the spherical mirror and was focused on the FPA using a silicon lens. For higher resolution (∼0.75 mm) imaging with a reduced field-of-view, the beam reflected from the spherical mirror was further focused using an off-axis parabolic reflector and silicon lens before reaching the FPA. In this case the object plane, located between the parabolic reflector and silicon lens, was significantly closer to the imaging plane. Figure 3 shows a photograph and THz transmission images of a dried seed pod obtained using these two configurations, acquired with 1 s of integration time. At a frame rate of 20 fps the imaging SNR was ∼2.5, increasing to ∼10 when averaged over 20 frames. It is worth commenting that this demonstration does not fully meet the requirements of a stand-off detection system, since the detector array is located no more than 3.25 m from the object plane in the two imaging configurations. Nevertheless, the acquisition of images over a path length >25 m in air represents an important milestone towards the development of long-range stand-off imaging systems. With the use of appropriate optical elements, such systems should be readily achievable, albeit at the expense of imaging resolution owing to the need for longer focal length optics.

In this section we have discussed how key characteristics of THz QCL sources such as their high power, sub-200 μm wavelengths, and narrow linewidths that can be tailored across the range 1.2–5.2 THz have facilitated the development of imaging systems exhibiting high dynamic range, fast acquisition rates, high transverse resolution and long-range capability. In sections 3 and 4 we consider how the ability to tune single QCL devices within the frequency range extending beyond 2 THz enables spectroscopic measurements in the frequency domain to be combined with these imaging capabilities.

3. Multiple-frequency THz QCL-based transmission imaging for spectroscopic analysis

It is known that crystalline materials exhibit a range of bonding strengths originating from both inter- and intra-molecular

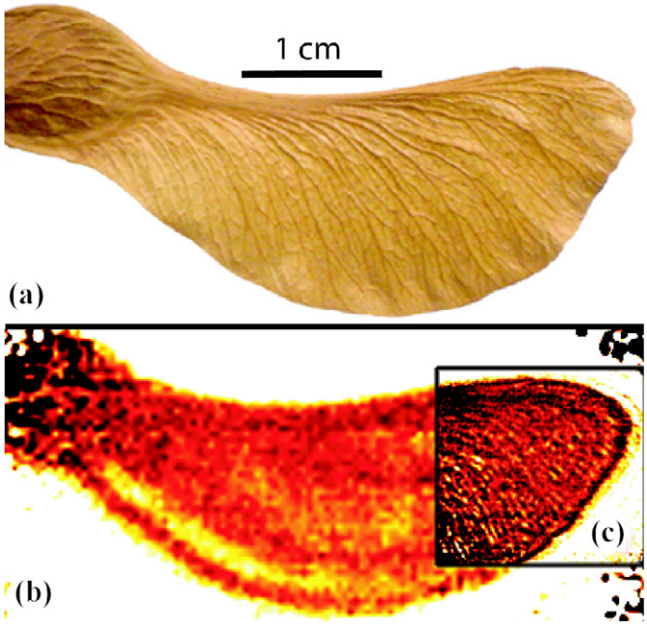

Figure 3. (*a*) Photograph of a dried seed pod. Corresponding THz images (averaged over 20 frames) acquired over an imaging distance of 25 m using a 4.9 THz QCL and FPA: (*b*) low-resolution imaging configuration, and (*c*) high-resolution imaging configuration. Reproduced with permission from [67]. Copyright 2006, AIP Publishing LLC.

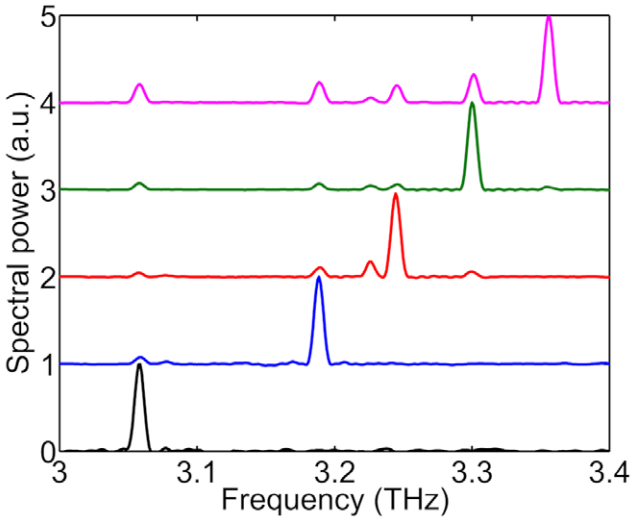

Figure 4. Normalized emission spectra obtained using a QCL based on a heterogeneous active region for five different biasing conditions (from bottom to top: 14.0, 15.6, 16.2, 16.5 and 17.2 V). Spectra were measured at a heat sink temperature of 15 K using 2 μs driving pulses. The device dimensions are 2.1 mm $\times$ 140 μm $\times$ 10 μm. (Adapted with permission from [71]).

interactions [11, 12, 85]. In the THz frequency range, these normal modes consist of contributions from rigid body rotation, centre-of-mass motion, and also internal vibrational modes. Their precise frequencies are highly sensitive to the chemical structure, and particularly to the long-range order within the crystal. As such, many crystalline solids exhibit unique spectral features at THz frequencies, which are often a combination of several normal modes. This allows samples to be discriminated chemically using THz radiation, and when combined with imaging capability enables chemical mapping of samples in two or three dimensions. Such demonstrations have previously been reported using time-domain TPI systems [13, 14, 17, 18] as well as frequency-domain approaches [15, 16]. The THz QCL is particularly suited to such applications due to its ability to deliver high spectral power densities at target frequencies greater than 3 THz where many materials exhibit spectral absorption features. However, THz QCL sources typically exhibit only limited tunability, accomplished through control of either the operating temperature or driving bias. Nevertheless, over recent years a number of schemes have been reported that provide extended tunability from QCL sources [37]. These include external cavity [86, 87] and coupled microcavity [88] devices, optomechanically coupled QCLs [89], as well as electrically switchable QCLs based on bi-directional [90] active regions and stacks of electrically switchable lasing units incorporated in the same device [91].

Another approach to achieving electrical tunability in THz QCLs has been based on the sequential stacking of multiple active region designs in a single device. In one structure, which was based on the three-well resonant-phonon active region as described elsewhere [92], the growth rate of gallium was reduced systematically by ~10% during epitaxial growth. This resulted in a 'heterogeneous cascade' active region in which the thickness of the GaAs wells was reduced by ~10% through the structure. In this type of design the lasing transition gradually shifts to higher energies throughout the structure, requiring application of greater electric fields to accomplish alignment of the energy levels and hence achieve lasing. By varying the applied bias, sequential switching of different lasing units therefore occurs, resulting in frequency tuning. This tuning effect has been exploited in a demonstration of multiple-frequency imaging [40] using a device based on this structure and processed in an SP ridge waveguide. Figure 4 shows the emission spectra of the device recorded for five different driving biases, resulting in emission predominantly at frequencies of 3.06, 3.18, 3.24, 3.30 and 3.35 THz. Although these spectra were obtained at a temperature of 15 K, it is worth noting that this device lased up to a maximum temperature of 85 K, thereby opening up the possibility of liquid nitrogen cooling.

The imaging system used for multiple-frequency imaging was based on a simple transmission geometry. Briefly, radiation was collected from the QCL and focused through the sample using a pair of parabolic reflectors, and the transmitted radiation detected using a helium-cooled silicon bolometer. In this system the beam size in the sample plane was measured to be <1 mm at all lasing frequencies, with negligible astigmatic difference. The sample was mounted on a two-axis translation stage enabling raster-scanning of the sample through the beam focus. By synchronising this raster-scan with the switching of the driving bias, and by recording the detector response for each of the chosen biasing conditions, image acquisition at multiple frequencies could be performed with a single scan of the target. With 10 ms of signal integration time per pixel the dynamic range was measured to be ~47 dB.

Transmission images of pressed pellets with diameter 8 mm and thickness $L \sim 0.5$ mm were acquired initially at two frequencies; 3.05 and 3.24 THz. After normalising to the incident beam power, the mean transmittance through the sample at each of the imaging frequencies, $T_{3.05}$ and $T_{3.24}$, was obtained by sampling 400 image pixels from the centre of the pellet (corresponding to a region measuring 5 mm × 5 mm). This spatial averaging was necessary to reduce the effects of inhomogeneity within the pellets and also laser speckle. In this respect, the fast acquisition rate attainable using this frequency-domain imaging approach offers a significant benefit over TPI approaches. From the measured transmittance and known sample thickness, the attenuation coefficient for each imaging frequency could be obtained. Alternatively, by taking the difference of the natural logarithms of the measured transmittances, on a pixel-by-pixel basis, an image representing the difference attenuation $\Delta\beta = (\beta_{3.05} - \beta_{3.24})\, L$ for each pellet could be generated. Figure 5 shows these difference-attenuation images for pellets of pure lactose monohydrate, pure glucose monohydrate, pure sucrose, and the high-explosive pentaerythritol tetranitrate (PETN) diluted with polytetrafluoroethylene (PTFE) to 26% by volume (26 vol%). For the PETN pellet a positive pixel value is obtained, indicating weaker attenuation at 3.24 THz compared to 3.05 THz, which is consistent with the absorption spectrum of the same sample measured using broadband THz TDS. Indeed, the absorption spectrum for this material consists of a strong resonance at ~2.85 THz [93], giving rise to an absorption coefficient that decreases with increasing frequency in the range 2.9–3.7 THz. Conversely, for the three pellets of sugars the difference attenuations attain negative values, revealing weaker attenuation at 3.05 THz than at 3.24 THz. These observations are also in agreement with the TDS spectra measured for each of these pellets, which show increasing absorption between 3.0 and 3.3 THz [40]. It is worth noting that, although the pellets of glucose monohydrate and sucrose are not easily distinguishable in this image, this is merely a consequence of the colour scale adopted to mark the presence of PETN. Overall, it can be seen that the sign of $\Delta\beta$, which is determined predominantly from the absorption spectra of these materials arising from their specific chemical and physical structure, enables these samples to be readily distinguished from each other.

In a further demonstration of spectroscopic imaging using this system, transmission images of the PETN sample were acquired at five frequencies spanning the range 3.06–3.35 THz. These images are shown in figure 6, and figure 6(f) shows the attenuation coefficients obtained for this sample at each of the imaging frequencies. As can be seen, the values obtained by QCL imaging agree well with those measured using TDS. From this demonstration it is clear that frequency-tunable THz QCL sources offer real potential for the development of fast and sensitive frequency-domain imaging systems with spectroscopic capability. With further advancements in tunable THz QCL sources, practical spectroscopic analysis over bandwidths exceeding 1 THz may become possible.

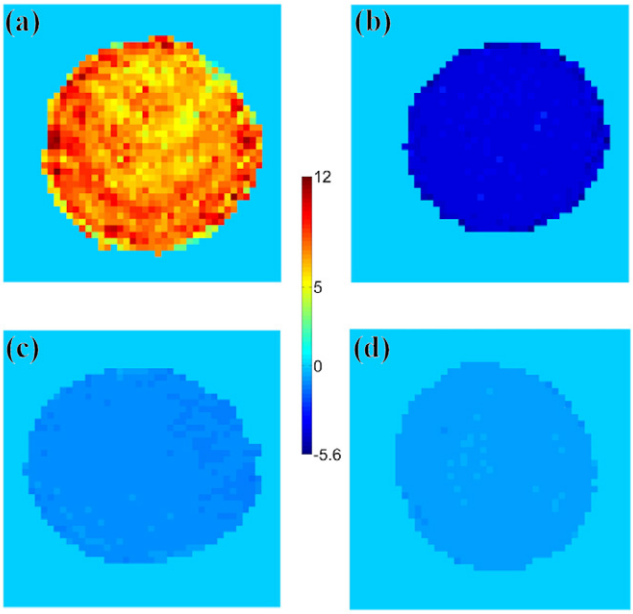

Figure 5. Difference-attenuation $\Delta\beta = (\beta_{3.05} - \beta_{3.24})\, L$ images of pellets of (a) 26 vol% PETN, (b) pure lactose monohydrate, (c) pure glucose monohydrate and (d) pure sucrose. The pixel intensity in image (a) has been multiplied by ten for clarity. Each image corresponds to an 11 mm × 11 mm area, and the step size is 250 μm. (Adapted with permission from [40], Copyright 2009 The Optical Society).

4. Multiple-frequency THz DRI

QCL-based imaging systems have usually employed transmission geometries owing to the reduced experimental complexity when compared with reflective imaging configurations. However, this approach typically precludes the investigation of highly absorbing samples such as bulky (thick) samples or those exhibiting high attenuation coefficients in the THz frequency range. As such, for highly absorbing samples an imaging configuration that collects radiation backscattered or specularly reflected from the sample is required. The capability to spatially map diffusely scattered radiation is also more applicable for practical stand-off imaging systems in which the precise alignment requirements for the collection of specular reflections from samples cannot be guaranteed.

DRI approaches are also particularly suited to the imaging of powdered samples for which a strong component of radiation scattered from beneath the surface of the powder can be expected. The mechanisms relevant to the interaction between radiation and powdered materials have been discussed elsewhere [60]. Notably, the strength of the diffusely scattered component is determined not only by the particle size of the powder relative to the radiation wavelength but also by the complex refractive index of the material, which governs the degree of absorption experienced by incident radiation that penetrates beneath the surface of the sample. This enables DRI techniques to be applied to the analysis of the absorption coefficient of targets, which is a crucial requirement of chemical mapping and fingerprinting applications. This incoherent approach thereby provides a practical and highly applicable alternative to coherent modalities in which the

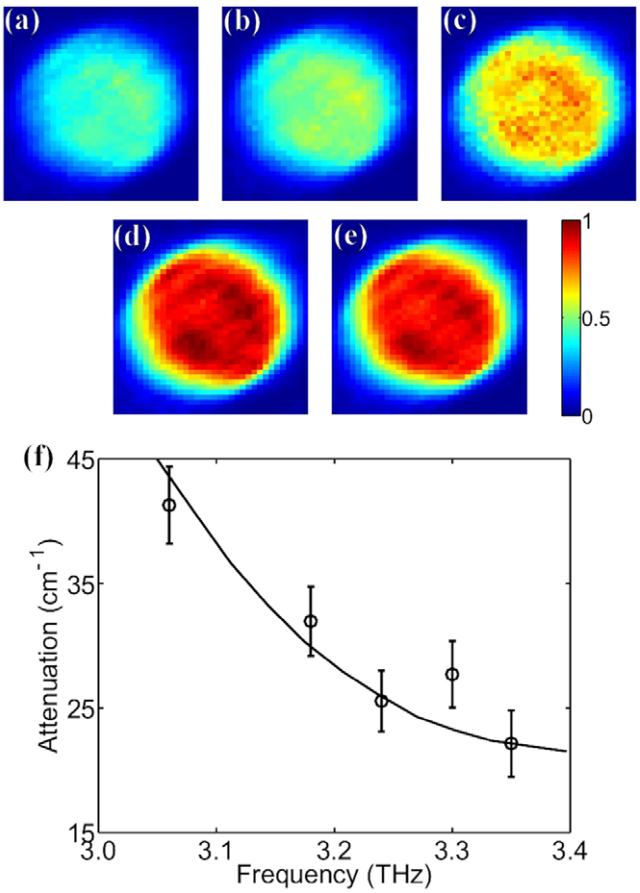

Figure 6. Normalized transmission images of a pellet of 26 vol% PETN acquired at imaging frequencies of (*a*) 3.06 THz, (*b*) 3.18 THz, (*c*) 3.24 THz, (*d*) 3.30 THz and (*e*) 3.35 THz using a QCL device based on an electrically switchable heterogeneous active region. The total image area is 11 mm × 11 mm (44 × 44 pixels). (*f*) Attenuation coefficients (circles) obtained from these images as a function of frequency. The error bars have been calculated from the variance of the 20 × 20 pixels sampled from each image. The corresponding attenuation spectrum measured using broadband THz TDS is also shown (solid line). (Adapted from [71]).

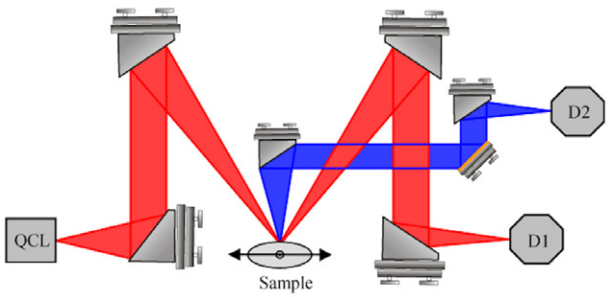

Figure 7. Experimental apparatus for simultaneous specular (red) and diffuse (blue) THz reflection imaging. D1—room-temperature pyroelectric sensor; D2—helium-cooled silicon bolometer. The sample is raster-scanned in two dimensions with a 250 μm step size using a two-axis translation stage. (Adapted with permission from [61], Copyright 2008 The Optical Society).

imaginary component of the refractive index is deduced from the phase shift incurred on Fresnel reflection from the target surface [94, 95].

Figure 7 shows an experimental arrangement for DRI using a bound-to-continuum QCL emitting at ∼2.8 THz [61]. Radiation from the source was focused onto the sample at an angle of 60° relative to the surface plane, resulting in a beam size measuring ∼350 μm × 305 μm on the sample surface. A parabolic reflector, matched to that used for focusing the incident beam, was employed to collect specular reflections from the surface of the sample, which were monitored using a room-temperature pyroelectric detector (D1). For collecting diffusely scattered radiation and non-directional radiation reflected from rough sample surfaces, a second set of optics in an off-axis collection geometry was employed. This weak diffuse signal was monitored using a helium-cooled silicon bolometer (D2). By raster-scanning the sample in two dimensions this system thus enables the simultaneous acquisition of images representing radiation both scattered and specularly reflected from samples. In this demonstration ∼400 μW average power was incident on the sample and an image acquisition rate of ∼170 pps was achieved. Using a weakly absorbing powder as a target, for which ∼1 μW of THz power is coupled to the bolometer, a dynamic range of 20 dB has been measured for this diffuse signal.

The applicability of this DRI scheme to the spatial mapping of powdered materials was initially demonstrated using exemplar powdered admixtures of polymethyl methacrylate (PMMA) and polystyrene. PMMA exhibits strong absorption in the THz frequency range whereas polystyrene is only weakly absorbing. Nine admixtures with equally spaced mass fractions in the range 0 to 1 were loosely packed inside a sample holder comprising a polystyrene box divided into 10 mm-deep compartments and fitted with a polystyrene lid (see figure 8(*a*)). Figure 8(*b*) shows the THz specular image of this sample, which predominantly shows strong specular reflections off the flat lid of the sample holder, whereas the powders are not resolved. The equivalent image obtained by DRI is shown in figure 8(*c*). In this case, the contribution from specular reflections is negligible and the image clearly reveals the powders. Furthermore, the image intensity corresponding to the nine powdered admixtures is strongly correlated with the mass fraction of highly absorbing PMMA material. This correlation is confirmed in figure 8(*d*), which shows the sample reflectivity R_∞ measured for each of the nine volume fractions of PMMA. By virtue of the PMMA and polystyrene powders having similar particle sizes (∼5–6 μm) and comparable refractive indices at 2.8 THz (∼1.38–1.42), similar scattering strengths can be expected from each of the nine admixtures. As such, the observed variation in sample reflectivity can be attributed predominantly to differing amounts of absorption within the samples. The values of R_∞ shown in figure 8(*d*) were obtained from the average image intensity sampled over a 20 × 20 pixel region (corresponding to 5 mm × 5 mm area) from the centre of each compartment, in order to reduce variations arising from laser speckle and structural inhomogeneity of the samples. In this respect, the ability to acquire diffuse reflection images, rather than sampling a single position on the target, is crucial to this technique.

A number of scattering models have been applied to the determination of absorption coefficients from DRI data,

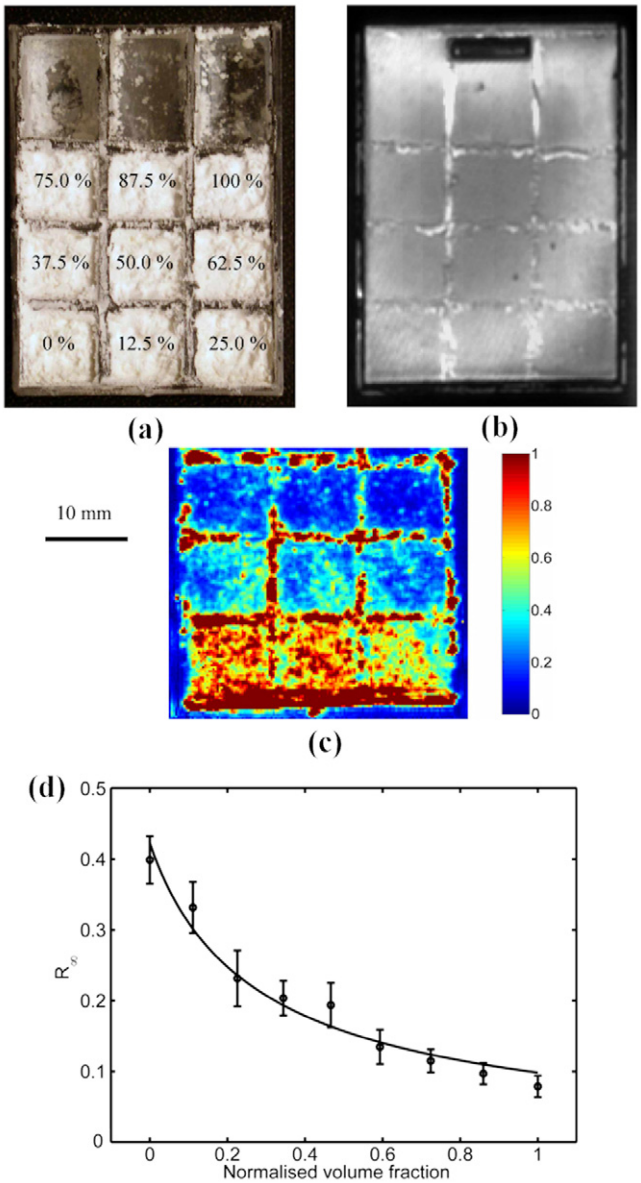

Figure 8. (*a*) Photograph of a polystyrene sample holder containing admixtures of PMMA and polystyrene powders. The % mass of PMMA is labelled for each powder. (*b*) Specular and (*c*) diffuse reflection images of the sample shown in (*a*), acquired at a frequency of 2.8 THz with a pixel size of 250 μm. (*d*) Sample reflectivities R_∞ obtained from the diffuse reflection THz image shown in (*c*), as a function of volume fraction of PMMA. The error bars have been calculated from the variance of the 20 × 20 pixels sampled for each powder. (Adapted with permission from [61], Copyright 2008 The Optical Society).

including the Kubelka–Munk theory and coherent scattering models such as the quasi-crystalline approximation (QCA) [96, 97]. For the imaging data shown in figure 8, the former of these theories provided an estimate for the absorption coefficient of PMMA equal to 42 ± 11 cm^{-1}, in excellent agreement with the value 41 cm^{-1} obtained by TDS. Nevertheless, such analysis requires knowledge of the *absolute* reflectance measured (or deduced) relative to an ideal (completely diffusing and non-absorbing) reference sample—conditions that cannot be achieved in practise. On the other hand, QCA-based scattering models require knowledge of sample parameters including particle size, volume fraction and refractive index for accurate determination of absorption coefficients. This requirement has been studied in detail elsewhere [98] using polydisperse powders, encompassing both pure and diluted polycrystalline powders as well as polymeric and amorphous materials, with arbitrary particle sizes, varying refractive indices, and a broad range of absorption coefficients that extend over two orders of magnitude over the range ∼3 to >200 cm^{-1}. Figure 9(*a*) shows an exemplar image containing samples of sucrose, lactose monohydrate, glucose monohydrate and polyethylene. For determination of absorption coefficients from this DRI data, the QCA was employed in conjunction with the Percus–Yevick pair distribution function [99]. As noted above, it was observed that the backscattering cross-section predicted under this model is strongly influenced by the complex permittivity of the sample. In particular, a larger real component of the permittivity (refractive index) induces stronger scattering of radiation from powdered samples owing to the greater resulting index contrast between the particles and surrounding air. For this reason, accurate determination of absorption coefficients from DRI measurements requires knowledge of the refractive index of the sample, through either estimation or measurement using complimentary techniques such as THz TDS. Figure 9(*b*) shows the relationship between the absorption coefficients obtained from DRI, α, and those obtained from TDS measurements on pressed pellet samples, α_{TDS}. As can be seen, when the material refractive index is accounted for correctly, good agreement is observed over the range of absorption coefficients studied.

It is worth noting that such restrictions on the use of scattering models for determination of *absolute* absorption coefficients from DRI data do not necessarily hinder the development of spectroscopic imaging systems based on this approach. In fact, for the purposes of identification or discrimination between materials including explosives and drugs-of-abuse, for example, it is only necessary to measure *relative* frequency-dependent changes in absorption. Furthermore, over narrow frequency ranges the real permittivity (refractive index) of most targets can be expected to remain approximately constant whereas the imaginary permittivity (absorption coefficient) can vary substantially. Any frequency-dependent variation of diffuse reflectance can therefore primarily be attributed to the absorption spectra of materials.

It is possible to extend DRI techniques to multiple frequencies through the use of a tunable THz QCL. Although THz QCLs are typically restricted to a continuous tuning range of a few GHz, a heterogeneous cascade structure [92] (as discussed in section 3) was used as a radiation source to provide discrete tuning over a wide range of frequencies. In this case, the QCL source emitted quasi-single-mode radiation at 3.06, 3.21, 3.28 and 3.35 THz, enabling images to be taken at four discrete frequencies. This source was used in the same DRI system described above and in [61], and was driven by a train of current pulses with 10 kHz repetition

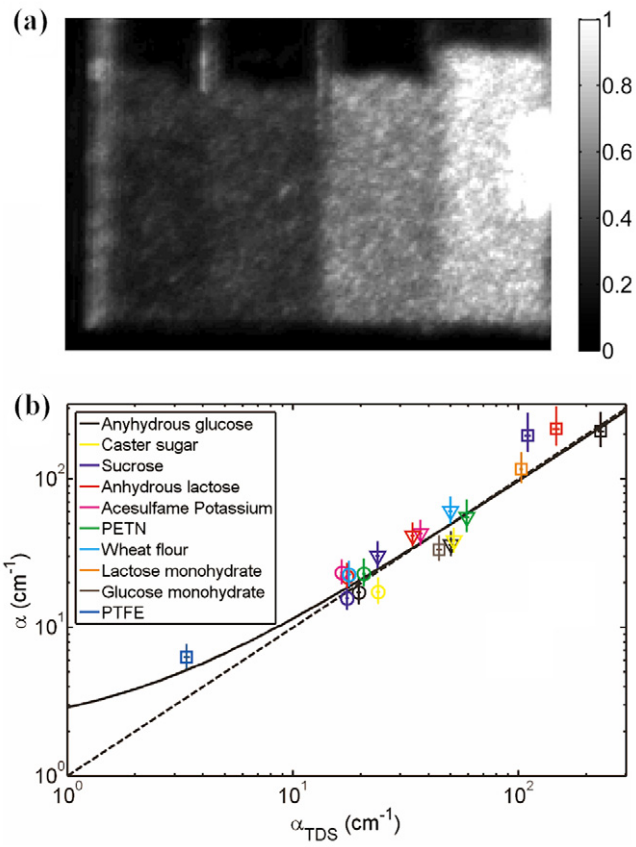

Figure 9. (*a*) Diffuse reflectance image of four bulk powdered samples (from left to right: sucrose, lactose monohydrate, glucose monohydrate and polyethylene) obtained at a frequency of 2.8 THz. The polystyrene sample holder comprises four compartments, with each compartment measuring approximately 10 mm wide, 30 mm tall and 10 mm deep. The bright region on the right of the image is a reflection from the lid of the sample holder. (*b*) Absorption coefficients α determined for a range of powdered samples using the QCA, plotted as a function of the absorption coefficient α_{TDS} obtained from TDS measurements. Samples shown include pure powdered samples (squares), 40 wt% samples (triangles) and 15 wt% samples (circles), diluted with polyethylene powder. The error bars have been estimated from the variance of the sampled image pixels. The dashed line indicates the relationship $\alpha = \alpha_{\mathrm{TDS}}$. The solid line shows the line of best fit $\alpha = 0.95\alpha_{\mathrm{TDS}} + 2.0\,\mathrm{cm}^{-1}$. Reproduced with permission from [98]. Copyright 2011, AIP Publishing LLC.

rate and 2% duty cycle. An image was acquired for each emission frequency by adjusting the drive current to obtain the maximum detectable power within each single frequency and then repeating the 2D scan. Although this frequency switching procedure multiplied the image acquisition time by ∼4, improvements could potentially be made by rapidly chirping the laser frequency and applying a time-division multiplexing scheme with a fast detector.

Figure 10 shows DRI images of a PTFE reference powder adjacent to samples of pure powdered sucrose and ammonium nitrate, obtained at each of the four lasing frequencies. The intensity of the diffuse reflections from the sucrose sample can be seen to decrease monotonically as the laser frequency increases, while the ammonium nitrate exhibits only a small change in its diffuse reflectance. As such,

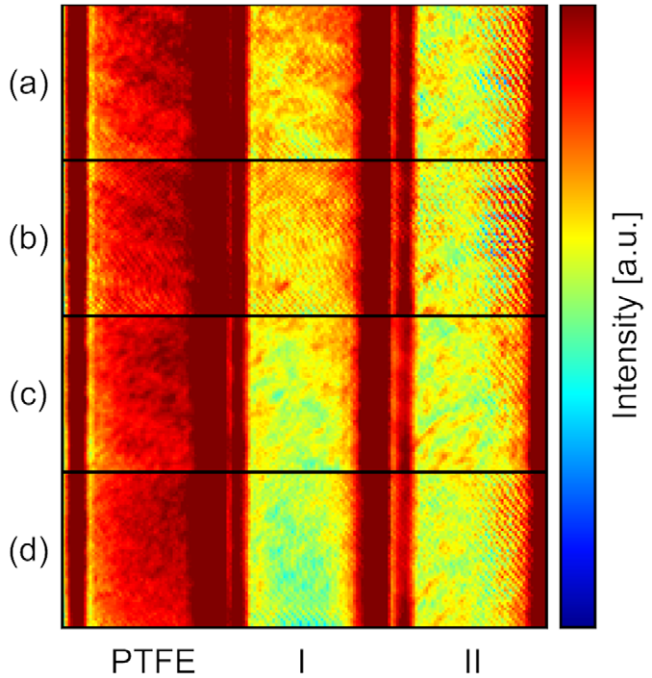

Figure 10. Diffuse reflectance image of three bulk powdered samples: PTFE; sucrose (I), and ammonium nitrate (II) obtained at frequencies of (*a*) 3.06 THz, (*b*) 3.21 THz, (*c*) 3.28 THz and (*d*) 3.35 THz.

it is possible to discriminate between materials using this technique. A number of methods are available to infer the Beer–Lambert absorption coefficient for a given material, although as discussed above, techniques such as the QCA or Kubelka–Munk models require prior knowledge of the properties of the material. Alternatively, a simple effective optical path-length (EOPL) model allows direct inference of the *relative* frequency-dependent changes in absorption within a material. Here, the absorption is assumed to take the form $\alpha = -\ln(R/R_0)/b\lambda$, where R and R_0 are the diffuse reflectance of the sample and non-absorbing reference material respectively, λ is the wavelength and b is a fitting parameter that represents the average path length of the THz radiation through the powdered medium. Although this model is insensitive to the geometry of the particles or the polarization of the incident radiation, it offers a simple means of comparing the DRI spectral data with that obtained using TDS techniques. The model was applied to the sucrose samples by tabulating the TDS absorption coefficient against the DRI reflectance of sucrose–PTFE admixtures with a range of concentrations. A frequency-independent path-length parameter of $b = 0.60 \pm 0.06$, was obtained through linear regression analysis of this data. Figure 11 shows the TDS absorption coefficient (solid lines) and the absorption inferred using the EOPL model for sucrose samples with 100% and 15% concentrations. It can be seen that the model reproduces the line shapes and the relative values of absorption coefficient accurately at both concentrations. With further improvements in the tunability of THz QCLs, this method could be used to obtain spectral data over even greater bandwidths.

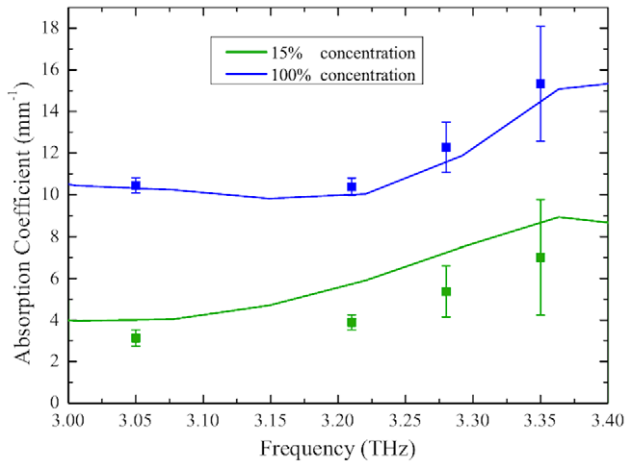

Figure 11. Absorption coefficients for pure sucrose and a 15% admixture with PTFE. Solid lines show the values obtained using THz TDS, while the symbols show values inferred from DRI measurements, using an effective optical path-length approximation.

5. Coherent imaging approaches

Until recently, imaging systems based on THz QCLs have almost exclusively relied on incoherent detection methods, most commonly through use of thermal detectors. The advancement of coherent detection schemes over recent years [49, 100], however, has made possible the development of coherent imaging systems exploiting QCL technology. Owing to the high power spectral density of QCL sources, such schemes offer the potential of extremely high dynamic range and detection close to the shot-noise limit [39, 100]. The ability to resolve both the amplitude and phase of the THz field also opens up the possibility of depth-resolved (3D) imaging [38]. Similarly, the phase and amplitude information can be related to the complex permittivity of the target in the same manner as in time-domain approaches such as TPI [95]. Capabilities such as these are set to further establish QCL-based imaging as a viable alternative to TPI.

Frequency-domain approaches to coherent detection require mixing the THz field with a reference signal derived from a local oscillator in order to generate an intermediate frequency (IF) suitable for electronic detection. A further requirement for achieving suitable phase stability of the IF signal is a frequency-stable THz source. Despite THz QCLs having recently been shown to exhibit sub-kHz quantum-noise-limited linewidths [36, 79], they suffer from a $\sim 1/f^2$ electrical and thermal noise component that leads to line broadening and frequency drifts. Thermal drift, in particular, can result in frequency drifts on the order of several MHz over time scales of seconds [80–82]. It is therefore often necessary to employ frequency stabilization of the QCL in coherent detection schemes. Invariably this involves use of a suitable feedback loop for dynamic control of the laser drive current and/or temperature [101, 102].

One approach to coherent imaging has employed frequency stabilization to a free-running CO_2 laser-pumped molecular laser emitting at 2.41 THz [59]. An IF signal was generated in this case by mixing the laser fields on a Schottky mixer at an offset frequency of 1.05 GHz, generated by an RF source. With the QCL stabilized, the molecular laser could then serve as a local oscillator for coherent detection of a portion of the QCL field returned from a target. For this 'imaging arm' of the system a second Schottky mixer was used. The experimental arrangement for this coherent imaging scheme is shown in figure 12(*a*). In this demonstration, the coherent detection capability was exploited for ISAR imaging of exemplar targets. Central to achieving a good spatial resolution and noise figures in ISAR imaging is the phase stability of the signal. Despite achieving a stabilized QCL linewidth of 20–30 kHz, a phase drift of $\sim\pm 7^\circ$ was observed in the current example over the 40 min acquisition time, which arose primarily from mechanical and acoustic noise producing path length (and hence phase) variations in the system. Nevertheless, this phase stability was sufficient for demonstration of the ISAR technique. The target was fully illuminated using a bistatic configuration employing 4 inch diameter spherical mirrors, resulting in a beam size measuring $\sim$2.5 inches at the target. The target was scanned in both azimuth and elevation angles, with phase and amplitude data being recorded at each orientation. By Fourier transform of this angular data, a 2D azimuth-range image of scattering centres could then be generated. Figures 12(*b*) and (*c*) show a photograph and azimuth/elevation THz image of a plastic model tank coated with aluminum. For this image the target was rotated from -2° to $+3.8^\circ$ in elevation, with a step size of 0.028°, and from -4.8° to $+4.8^\circ$ in azimuth, with a step size of 0.02°. This scanning range corresponds to pixel resolutions of 0.4 and 0.6 mm in these two directions. The resulting acquisition time was 40 min, and the dynamic range for each pixel was measured to be $\sim$105 dB. It is worth noting that, as well as providing a large dynamic range, this ISAR scheme is particularly suited to high-resolution long-range imaging. As pointed out in [59], in order to achieve a 1 mm spot size at a stand-off distance of 20 m at 1.5 THz, a 5 m diameter reflector would be required. Conversely, in ISAR imaging the resolution is determined by the angular extent of the scan. Thus the target can be fully illuminated by a large beam whilst still achieving sub-mm resolution.

An alternative demonstration of coherent imaging has used a scheme whereby the THz QCL is stabilized to a near-infrared fs-laser comb [39]. In this scheme, which was based on an earlier demonstration with a Gunn oscillator emitting at 600 GHz [25], the THz field was sampled on an electro-optic (EO) crystal using a frequency-doubled mode-locked fs-fibre laser operating at 780 nm. This enabled the QCL to be stabilized to a high harmonic ($\sim 10^4$) of the 250 MHz laser repetition rate. A stabilized beat signal with an SNR of 80 dB in a bandwidth of 1 Hz has been achieved using this approach with a 2.7 THz QCL [100]. In a manner similar to the system described above, a portion of the fs-laser comb could also be used as a reference signal for coherent sampling of the THz field reflected from a target, using a second EO sampling arrangement (EO2). The schematic diagram for this coherent imaging scheme is shown in figure 13(*a*). The RF frequencies f_{RF1} (=10 MHz) and f_{RF2} (=10.07 MHz) were used to frequency-offset the beat frequency f_{beat} generated at

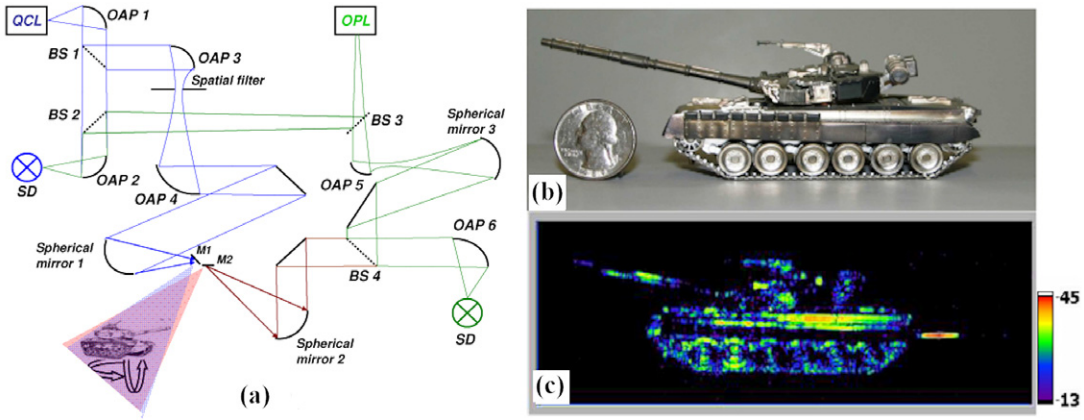

Figure 12. (*a*) Experimental apparatus for ISAR imaging using a THz QCL. OAP—off-axis parabolic reflector; BS—beam splitter; SD—Schottky detector; OPL—optically pumped THz laser emitting at 2.41 THz. (*b*) Photograph and (*c*) azimuth/elevation image of a plastic model tank coated with aluminum, taken at 2.4 THz. The amplitude values in dB are indicated by the colour scale. The THz image resolution is 0.4 × 0.6 mm. (Adapted with permission from [59], Copyright 2010 The Optical Society).

EO1, and to later down-convert f_{beat} to the operating range of the lock-in amplifier. For the 'imaging arm' a noise floor of −140 dBm (1 Hz bandwidth) was reported, determined by shot noise in the optical photodetector, which corresponds to a small NEP of only $\sim$3 pW Hz^{-1}. A phase stability of $<3^{\circ}$ h^{-1} was reported, again limited by mechanical stability rather than frequency drift of the QCL. Figure 13(*c*) shows an unwrapped phase image acquired from a portion of a 10 cent Euro coin, revealing the different target depth for the numeric characters relative to the flat surface of the coin. The corresponding power image is shown in figure 13(*b*). In addition to enabling phase-sensitive imaging, one of the benefits of this approach is that the THz field is up-converted to near-infrared frequencies, thereby enabling the use of well-established near-infrared/visible detector technologies for THz detection. Of particular note is the possibility for full-field EO image capture [65] using demodulating detector arrays [103, 104].

Despite the benefits offered by these coherent imaging systems, they nevertheless suffer from complex experimental setups involving multiple laser sources, and separate detector arrangements for laser stabilization and imaging. Recently, however, we have reported a coherent imaging approach based on the phenomenon of SM in a THz QCL that overcomes these concerns. Recent progress within this emerging field is summarized in the following section.

6. Coherent imaging through SM in a THz QCL

6.1. High-resolution imaging over extended distances

SM occurs when radiation emitted from a laser is partially reinjected back into the laser cavity from an external target. The reflected radiation interferes with the intra-cavity field, causing measurable changes to the optical and electrical properties of the laser that depend on both the amplitude and phase of the returning field [105, 106]. By this means, a single laser device may act as both radiation source and coherent detector, enabling the realization of simple and compact experimental arrangements. Despite motivating significant research interest in visible and near-infrared lasers [107], the SM effect has only recently been studied in THz QCLs. Nevertheless within the last few years SM sensing has been applied to measurement of the linewidth-enhancement factor of THz QCLs [108, 109], for studying the intrinsic stability of QCLs under optical reinjection [110], for THz displacement-sensing [109], and for THz imaging of free carriers on the surface of semiconductors [111].

In visible and near-infrared lasers, SM signals are commonly observed via the emitted laser power, typically using a photodetector integrated within the laser package [107]. However, an alternative approach, better suited for the THz range, is to monitor the SM signal via the voltage variation across the laser terminals. In addition to reducing the size and complexity of THz imaging systems, this approach also enables extremely fast detection since the speed of response to optical feedback is fundamentally determined by elastic and inelastic scattering mechanisms that occur on picosecond time scales in THz QCLs [112, 113], thereby enabling response bandwidths on the order of $\sim$10–100 GHz, in principle. A further advantage of this approach that is highly applicable to the development of THz imaging systems is the potential for implementation in sensing arrays [114].

The experimental arrangement of our simple SM imaging system is shown in figure 14. In this demonstration the THz QCL was based on a bound-to-continuum active region [115] emitting at 2.6 THz and was driven in cw at a constant current of 900 mA, just above the lasing threshold. Radiation from the QCL was focused onto the target using a pair of $f/2$ off-axis parabolic reflectors and similarly coupled back into the laser cavity after reflection from the target. In this system, $\sim$240 μW was delivered to the sample. An optical chopper was employed to mechanically modulate the beam, with the corresponding modulation to the QCL voltage (the SM signal) being recovered using a ×100 ac-coupled differential amplifier and lock-in amplifier. It is worth noting that this optical arrangement is self-aligning by nature and also intrinsically confocal due to the requirement of coupling radiation back into the narrow laser aperture. The spatial resolution of this system was determined to be better than 250 μm. Figure 15(*a*)

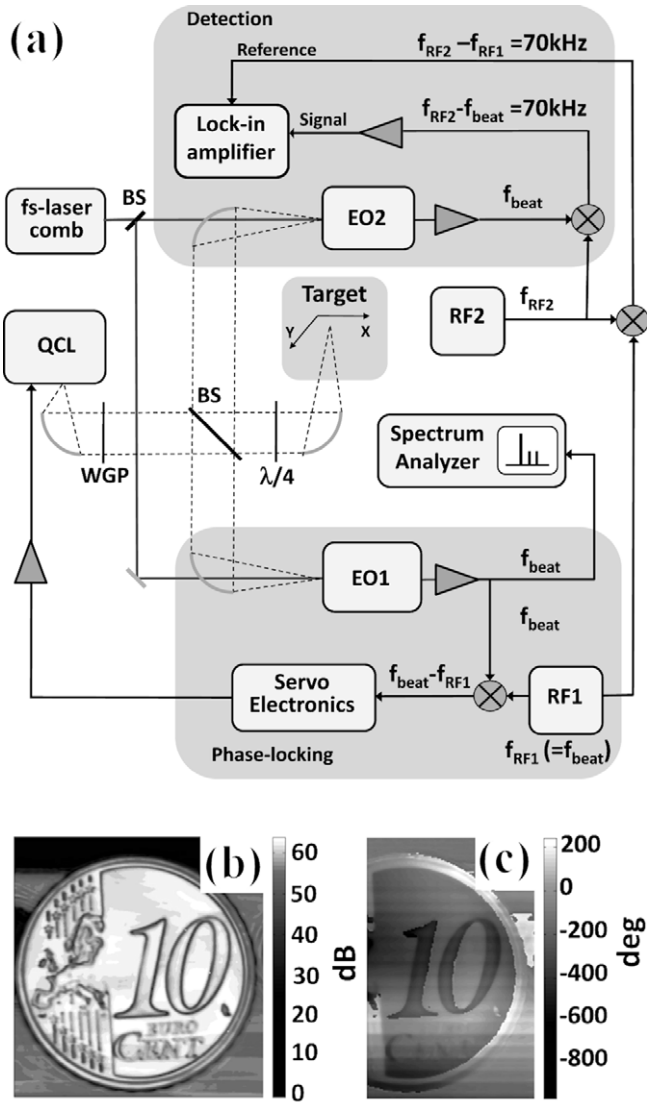

Figure 13. (*a*) Experimental apparatus for coherent imaging using a THz QCL stabilized to a near-infrared fs-laser comb. EO1 and EO2—stabilization/phase-locking and imaging/detection EO sampling units, respectively; BS—beam splitter; WGP—wire grid polarizer; $\lambda/4$—THz quarter-wave plate. The WGP and $\lambda/4$ form an optical isolator to prevent feedback of radiation to the QCL cavity. The target is raster-scanned in the $X-Y$ plane. Images of a coin with diameter 19.75 mm, taken at a frequency of 2.5 THz, showing the (*b*) THz power and (*c*) unwrapped THz phase. The image pixel size is 100 μm. Reproduced with permission from [39]. Copyright 2013, AIP Publishing LLC.

shows an exemplar high-resolution image of a UK two-pence coin acquired using a step size of 100 μm.

By inserting calibrated attenuators between source and target, this non-optimized system has been shown to tolerate ~48 dB of signal attenuation, corresponding to a detectable reflected power of less than 4 nW. This high sensitivity has enabled imaging over extended distances. Figure 15(*b*) shows an image of a scalpel blade acquired over a round-trip path length of 21 m, achieved by folding the THz beam using planar mirrors inserted between the parabolic reflectors. A figure-of-merit for the dynamic range of this image can be defined as $K = (\mu_f - \mu_b)/\sigma_b$, where μ_f is the mean SM

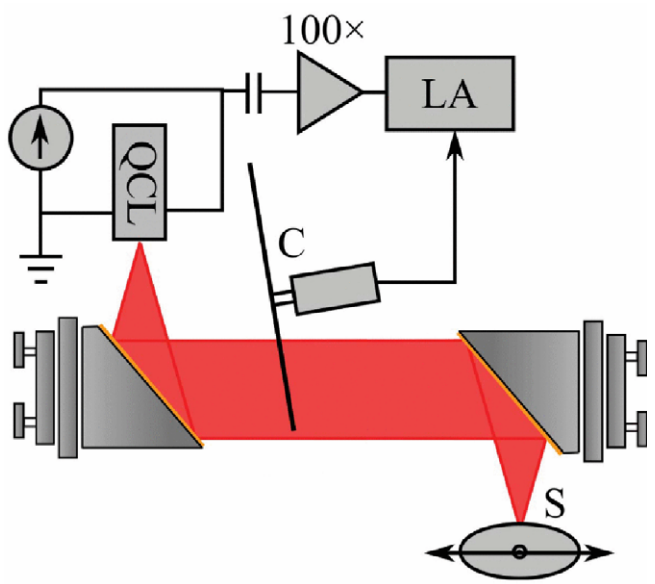

Figure 14. Experimental apparatus for imaging using the SM effect in a THz QCL, by monitoring the QCL terminal voltage. LA—lock-in amplifier; C—mechanical chopper. The sample S is raster-scanned in two dimensions with the lock-in amplifier output being recorded at each position.

voltage acquired over a flat part of the blade that corresponds to a fringe maximum in the image, and μ_b and σ_b are the mean and standard deviation of the SM voltages recorded over the background of the image [84]. For this long-range image we obtain a value $K = 43.5$; only slightly lower than the value $K = 61.5$ obtained for a comparable short-range (1 m round-trip) image (not shown). Whilst these figures-of-merit are likely influenced by the specific system alignment in each of these cases, this result nevertheless suggests that even longer imaging ranges may be possible using the SM approach. Indeed, based on an instantaneous free-running linewidth $\Delta f \sim 20-30$ kHz [55, 80, 81], the coherence length of a THz QCL, which determines the maximum path length for coherent detection, is estimated to be $L_c = c/\Delta f \approx 10$ km in vacuum.

6.2. Two-dimensional imaging by electrically modulated SM sensing

Due to the cw nature of the SM arrangements described above, a mechanical chopper is commonly used to enable lock-in detection of the relatively weak (~mV) SM response that is superimposed on the QCL terminal voltage. However, this mechanical modulation imposes an upper limit (~200 Hz) on the modulation frequency, which is far below the ~10–100 GHz optical feedback response bandwidth of QCLs. This bottleneck may be overcome through the use of electrical modulation schemes for 2D and 3D imaging.

The electrical modulation technique described here uses a dc driving current just below the lasing threshold, with a square wave modulation used to drive the QCL above threshold, thereby modulating the SM signal. This not only reduces the number of optical components, but the modulation frequency is no longer mechanically limited, thereby enabling

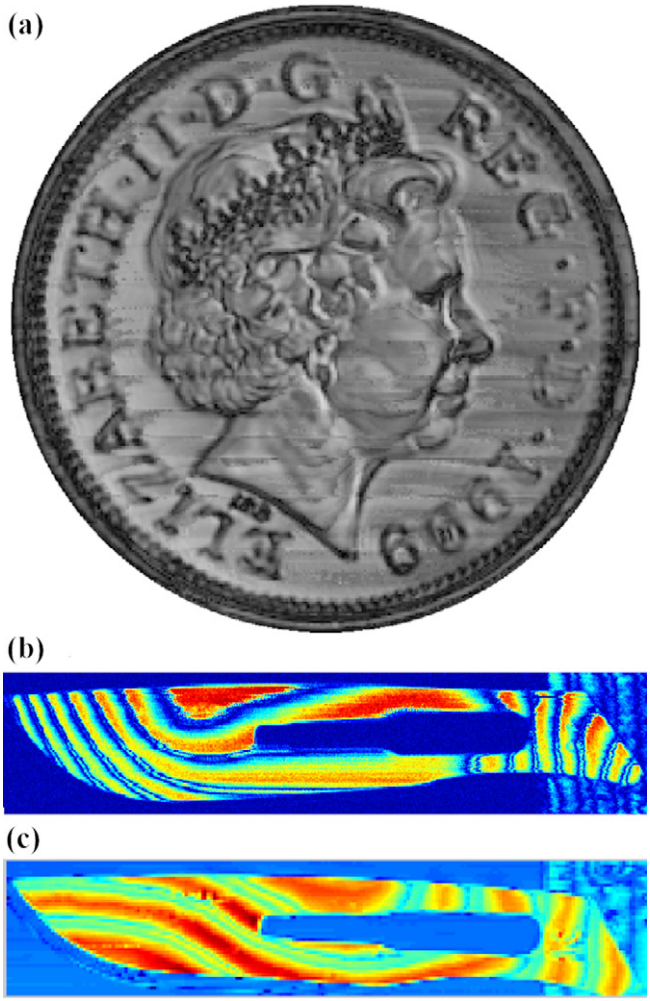

Figure 15. Images obtained by SM in a QCL emitting at 2.6 THz. (*a*) A high-resolution image of a UK two-pence coin (diameter = 25.9 mm) and (*b*) an image of a scalpel blade acquired with a round-trip path length of 21 m through air. Images (*a*) and (*b*) were acquired using mechanical modulation of the THz beam. (*c*) Image of a scalpel blade obtained using electrical modulation of the QCL at a frequency of 60 kHz. The image size is approximately 42 mm × 10 mm for both (*b*) and (*c*), but the images were acquired under different system alignment. The step size is 100 μm for all images. (Adapted with permission from [49], Copyright 2011 The Optical Society and [84], Copyright 2013 IEEE).

faster acquisition. By comparing images acquired using both mechanical and electrical modulation at 200 Hz we have found comparable image clarity with similar figures of merit K under equivalent measurement conditions. Specifically, with 50 ms integration per pixel, we have obtained $K = 140$ and 155 for mechanical and electrical modulation schemes, respectively. With the electrical modulation frequency increased by more than two orders of magnitude to 60 kHz a comparable value $K = 140$ was obtained (see figure 15(*c*)). For this higher modulation frequency it was also possible to decrease the acquisition time per pixel by a factor of ten, limited only by the acquisition hardware, with only a modest degradation in image quality ($K = 95$). At higher frequencies the SM signal amplitude was found to degrade due to the modulation frequency limit of the laser driver, although we anticipate that the modulation frequency could in principle be increased far beyond this range, enabling significantly greater acquisition rates. A natural extension to this approach would be to form the modulating square wave by alternating the QCL driving current between two different levels, both above the lasing threshold. This could create an SM signal at two lasing frequencies and consequently two different phases of the reinjected electric field. Therefore, the two levels of alternating driving current of this electrical square wave modulation may, for example, be tuned to create the reflected waves perfectly out-of-phase leading to high contrast in the resulting SM signal levels.

The SM phenomenon is fundamentally coherent in nature, and so SM signals naturally depend on the phase of the electric field coupled back into the laser cavity. As the imaging position on the target changes, the length of the external cavity may also change leading to the light and dark fringes observed in figures 15(*b*) and (*c*). These fringes reveal the surface morphology of the blades, with adjacent fringes corresponding to a longitudinal displacement of half a wavelength, or ~58 μm in this case. This coherent nature of the SM sensing approach has recently been exploited for 3D coherent imaging using a THz QCL [38].

6.3. Three-dimensional imaging through SM in a THz QCL

One experimental arrangement for 3D SM imaging has been based on the system shown in figure 14, but mounting the target on a computer-controlled translation stage thereby enabling longitudinal scanning with respect to the beam path. Through this approach the SM waveform could be captured synchronously at each transverse position on the target, enabling both the depth and reflectance of the target surface to be mapped in two dimensions thereby generating a 3D image. Coherent 3D imaging was performed on an exemplar GaAs structure that was fabricated by wet chemical etching. This sample comprised of three stepped regions (in the X-direction) with a nominal step height ~10 μm and a width (in the Y-direction) of 3.1 mm. The upper half of the structure was also coated with a 125 nm-thick layer of gold in order to provide regions of differing reflectance. For coherent image acquisition, the sample was scanned on a pixel-by-pixel basis through a longitudinal (z) distance of 0.5 mm, corresponding to nine interferometric fringes. With a lock-in time constant of 10 ms, the resulting acquisition rate was 20 s/pixel in this non-optimized demonstration.

Figure 16(*a*) shows typical SM waveforms acquired from different positions on the sample surface corresponding to gold-coated and uncoated regions on different steps, resulting in relative variation in both the phase and amplitude of the waveforms. The amplitude of the reflected THz wave, as well as the total phase accumulation within the external cavity formed by the target, were extracted from the SM signals by fitting to a three-mirror model of the laser under feedback [116]. As described elsewhere [38], the phase of the SM signal obtained in this manner can be related to the path length travelled by the THz radiation in the external cavity, and hence to the depth of the surface of the target δL. Furthermore, the amplitude of the SM waveform can be related to the sample

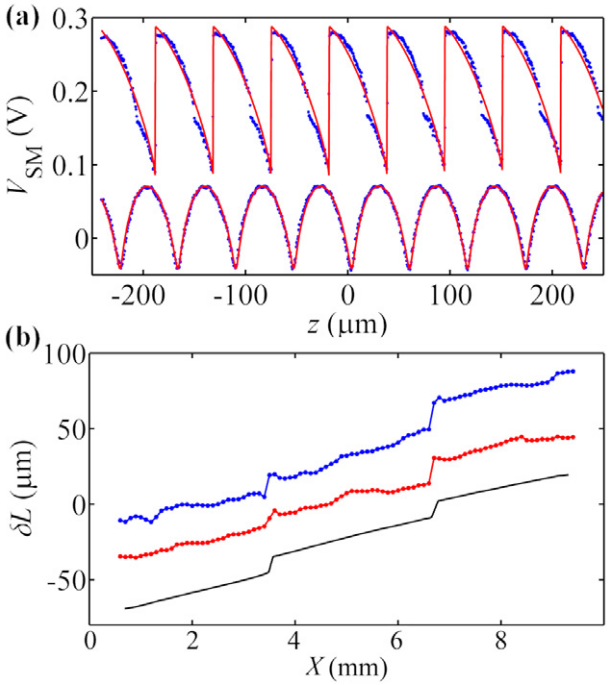

Figure 16. (*a*) SM waveforms (blue dots) obtained from two positions on the surface of a stepped GaAs sample. The red solid lines show fits to a three-mirror model describing the laser system under feedback. The upper trace corresponds to a region of the sample coated in gold. (*b*) Surface depths δL for the sample measured for one row of pixels (blue; top trace) and from the average of all rows (red; middle trace). Also shown is the sample profile obtained using a non-contact optical profilometer (black solid line; bottom trace). Each profile has been offset vertically for clarity. Reproduced with permission from [38]. Copyright 2013, AIP Publishing LLC.

reflectance. Figure 16(*b*) shows the surface depth δL obtained from the fits to one row of pixels traversing the three stepped regions of the sample and also the average depth variation obtained across all five rows of pixels. The etched steps can be resolved clearly, as can the tilt of the sample, which is estimated to be $\sim 0.4^\circ$. Also shown is the surface profile characterized using a non-contact optical profilometer (Bruker NPFLEX 3D), after correction to replicate the sample tilt measured from the SM signals. As can be seen, there is very good agreement with the THz depth profile. The corresponding 3D THz reconstruction of the sample is shown in figure 17(*a*), in which the colour scale indicates the depth of the surface.

Figure 17(*b*) shows the variation of the square of the fitted waveform amplitude across the surface of the sample. According to the SM model [38], this quantity varies as $\varepsilon^2 R$, in which R is the surface reflectance and ε is a coupling constant representing loss due to attenuation in the external cavity, spatial mode mismatch between the reflected and the cavity mode, and other optical losses due to factors including misalignment and scattering from rough surfaces. The top rows of pixels in figure 17(*b*), which correspond to the gold-coated region of the sample, clearly reveal the higher surface reflectance. However, it can be observed that the amplitude is not homogenous across each region. This is attributed to scattering from surface defects and variations in the sample geometry arising from the etching process, which cause deviations in the reflection angle of the beam and hence variation in the coupling constant ε across the surface.

It is worth reiterating that this coherent imaging approach is experimentally simple and compact, and does not require frequency stabilization of the QCL. As such we can estimate the resolution limit (noise-equivalent displacement) imposed by frequency instability by assuming a typical frequency drift ~10–15 MHz over the acquisition period [81, 82]. The resulting phase change of the SM waveform relates to an effective change in cavity length of $\sim 2\,\mu$m in this case, allowing small depth variations to be resolved.

6.4. Swept-frequency interferometric imaging for materials analysis

In all the demonstrations of coherent imaging using a THz QCL reported to date [38, 39, 59], the phase information encoded in the imaging data has been related to the geometry of the target under investigation. This approach is equivalent to time-domain techniques whereby the temporal delay of the THz wave, measured after reflection from a target, is interpreted in terms of the path lengths corresponding to reflective interfaces within the target. The characterization of coating thickness and uniformity in coated pharmaceutical tablets has been reported based on this technique [9, 11]. Alternatively, however, the phase change upon reflection from a target can be related to the complex permittivity of the target material. This is the basis of THz time-domain reflection spectroscopy [117], which enables THz frequency spectroscopic measurements on thick and/or highly absorbing samples including liquids [118]. The coherent nature of the SM approach has recently led to the development of an equivalent swept-frequency technique for both THz imaging and materials analysis in a reflective geometry [95]. Such application of a narrowband QCL source offers the advantage of high output power spectral density, spectral resolution exceeding that offered by TDS by several orders of magnitude, and the capability for high-speed measurements in a compact system.

In an SM imaging system the total phase shift incurred in one round trip of the beam comprises a contribution from the propagation phase shift corresponding to twice the optical path length of the external cavity, which we view as the optical length from the QCL source to the target and back to the QCL source, in addition to the phase shift occurring on reflection at the target. The former of these can be varied, resulting in a series of cavity resonances ('fringes') observable on the SM signal, by either varying the external cavity length or alternatively by applying a chirp to the laser frequency through ramp modulation of the driving current. For this latter frequency modulation approach the temporal separation between the SM fringes, as well as their shape and phase, depend on the external cavity length but also the complex permittivity of the target. Thus, through analysis of the SM waveform, the complex reflectivity of the target may be deduced. Using calibration standards, such an approach has recently been applied to the determination of the complex refractive indices of exemplar plastic materials with high accuracy [95].

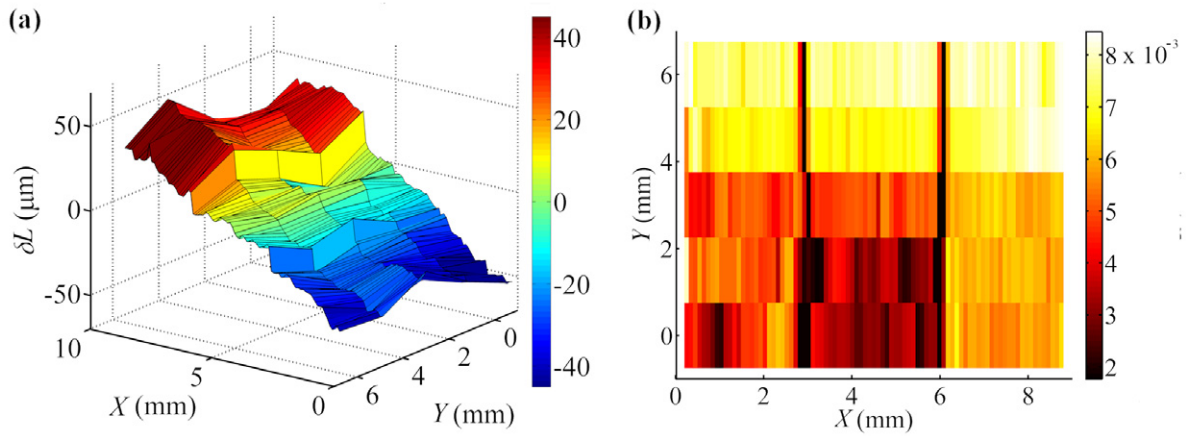

Figure 17. (*a*) 3D reconstruction of a stepped GaAs sample obtained by SM in a QCL emitting at 2.6 THz. The colour scale corresponds to the depth of the surface. (*b*) Square of the SM waveform amplitude measured across the surface of the sample, representing the effective surface reflectance $\varepsilon^2 R$. The upper two rows of pixels in (*b*) correspond to the region of the sample coated in gold. Reproduced with permission from [38]. Copyright 2013, AIP Publishing LLC.

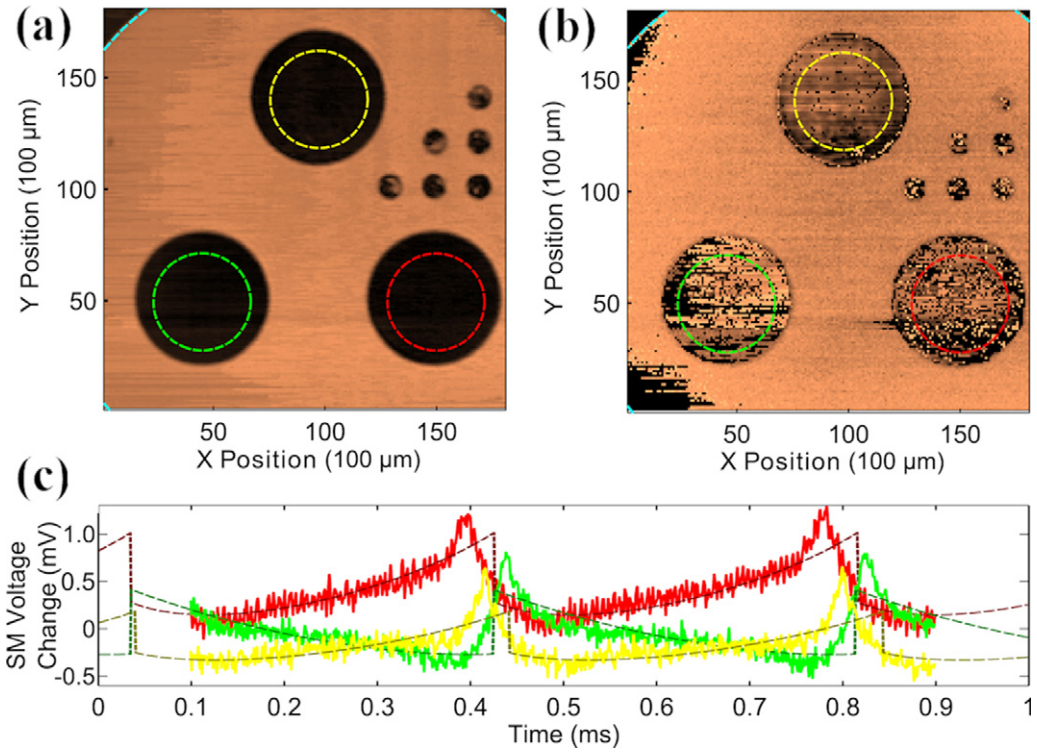

Figure 18. (*a*) Amplitude-like image of an aluminum cylinder containing three cylindrical bores of different plastics, obtained by swept-frequency SM using a QCL emitting at 2.59 THz. (*b*) Phase-like image of the same target. The three circular regions indicate the different materials under test: yellow—polycaprolactam; green—polyvinyl chloride; red—polyoxymethylene. (*c*) Representative time-domain waveforms obtained for a single spatial pixel on the target for each of the three materials (solid lines) with corresponding fits to the SM model (broken lines). The common reference slope has been removed. (Adapted with permission from [95], Copyright 2013 The Optical Society).

In this demonstration the laser was driven in cw just above the lasing threshold, with a sawtooth current modulation superimposed on the dc driving current; this 50 mA peak-to-peak modulation corresponded to a 600 MHz chirp of the emission frequency. For image acquisition, the time-domain SM waveform was recorded at each pixel using a digital acquisition card. From these waveforms, both amplitude and phase information could be determined on a pixel-by-pixel basis. Figure 18(*a*) shows an amplitude-like image of a custom-designed composite target consisting of a 1 inch aluminum cylinder equipped with three cylindrical bores (5 mm diameter) containing different plastics. In this image, the copper colour represents stronger feedback, which arises from the aluminum part of the target, whereas darker regions indicate weak feedback from the plastic bores. Due to the colour scale adopted here and the strong feedback from the

aluminum relative to the three plastics, the contrast between the different plastic regions is not immediately apparent from this image. Nevertheless, this amplitude contrast is preserved in the time-domain signals acquired for each plastic, as can be seen in figure 18(*c*). Also evident in these waveforms is the differing temporal shift of the SM signal relative to the rising edge of the modulation waveform. This phase-like representation of the SM waveforms is shown in figure 18(*b*). In combination, these amplitude and phase images reveal spatial changes in the magnitude and phase of the complex reflectivity of the target. In particular, through fitting the acquired SM waveforms to a model based on the steady-state solution of the Lang–Kobayashi equations [105], both the refractive index and the extinction coefficient of the target can be obtained on a pixel-by-pixel basis, following appropriate calibration of the model using materials of known complex index. This approach has been shown to enable measurement of material properties with high accuracy [95]. Among the attractive qualities of this SM approach is its compact form and its ability to enable coherent sensing via the laser terminal voltage without the need for an external detector. This technique could therefore be readily extended to arrays of THz QCLs operating at multiple frequencies, or single electrically switchable QCLs, thereby enabling spectroscopic material characterization and identification within a fast and sensitive high-resolution imaging system

6.5. High-resolution ISAR imaging by SM

As described previously, the majority of THz QCL-based imaging approaches acquire images by raster-scanning the sample through the focused THz beam (although notable exceptions have been discussed in section 2.3). The resolution of images formed in this manner is determined by the laser beam spot size, which depends on the operating frequency of the laser and the diffraction limits of the optical system. To overcome this limit, however, the coherent nature of SM in THz QCLs has recently been exploited for ISAR imaging, leading to spatial resolution exceeding the diffraction limit [119].

Key to the ISAR approach is the realization that the morphology of the SM signal is influenced by the spatial distribution of the reflection coefficient of the target across the illuminated region. Information about this distribution can be obtained by acquiring a series of SM signals from successive, partially overlapping spots on the target. Using the swept-frequency approach described in section 6.3, such a set of SM waveforms was acquired by raster-scanning a resolution target through the THz beam. From each of these waveforms the aggregate complex reflection coefficient corresponding to the illuminated part of the target was then obtained, enabling the relative magnitude and phase of the backscattered electric field at the QCL facet to be calculated. Finally, the resulting complex backscattered fields were processed using an ISAR matched-filter algorithm [120] to recover the spatial dependence of the complex reflectivity across the target surface with a high resolution.

Figure 19(*a*) shows the root-mean-square of the SM signal as a function of position across the resolution target,

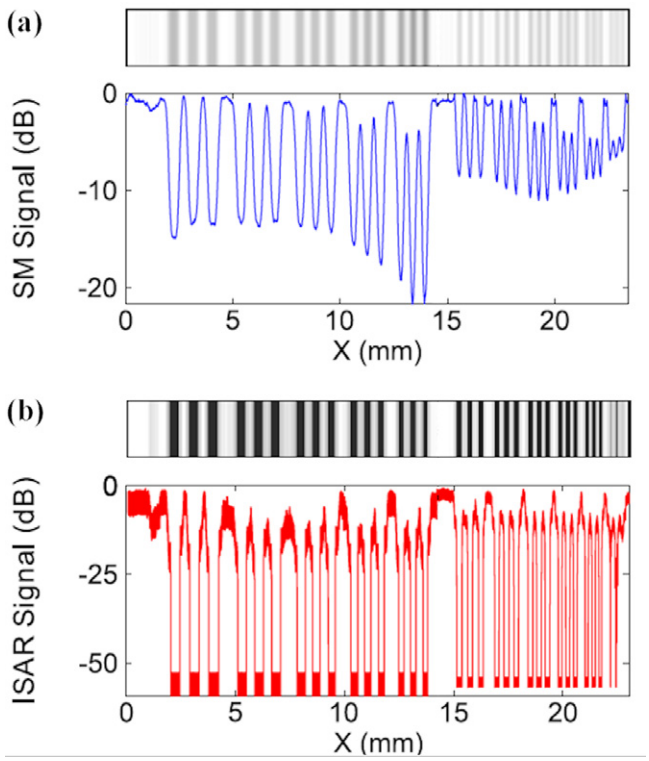

Figure 19. (*a*) One-dimensional SM image of a resolution target. The horizontal axis corresponds to the target position relative to the illuminating beam. (*b*) Processed ISAR image of the same target in which the horizontal axis corresponds to the position of the reconstructed scattering profile at the target surface. The resolution target size varies from 1.12 to 3.56 lppmm. (Adapted with permission from [119], Copyright 2014 The Optical Society).

demonstrating that the usual unprocessed raster-scanning approach is able to resolve features down to 3.56 line pairs per millimetre (lppmm). However, it can be seen that the image contrast decreases with increasing spatial frequency. Conversely, the image generated through the ISAR approach is shown in figure 19(*b*). It can be seen that the bars are more sharply resolved through the ISAR approach, with about 50 dB change in signal level being observed even for the thinnest bars. For comparison, a signal variation of only ∼2 dB is observed in the corresponding unprocessed image. From these results it is clear that the ISAR approach significantly improves the contrast and spatial resolution of SM images whilst retaining the high sensitivity and dynamic range inherent to coherent detection schemes.

7. Summary and outlook

The THz frequency QCL has now established itself as a compact, high power, spectrally pure source particularly suited to the application of THz imaging across a range of disciplines including biomedicine, security controls, industrial inspection, non-destructive analysis and spectroscopic mapping of materials. These sources offer tremendous benefits for THz imaging in terms of high dynamic range, high spatial resolution, potentially fast imaging rates and frequency tunability that can be applied to spectroscopic analysis of

targets. As such, these sources have motivated significant research interest over the past decade. Furthermore, despite the requirement for cryogenic cooling, the deployment of QCL sources within compact and turn-key systems has now become a realistic prospect [41–43, 49]. Within recent years, a number of coherent imaging approaches using THz QCLs have also emerged, most notably through use of the self-mixing effect in these lasers, which show remarkable stability under optical reinjection [110]. The benefits of coherent detection, coupled with the further development of QCLs capable of extended tuning, broader spectral coverage, higher output powers and higher operating temperatures now offer great potential for the future advancement of THz imaging technologies.

Acknowledgments

We are grateful for support from the EPSRC, the ERC (*NOTES* and *TOSCA* programmes), the Royal Society, the Wolfson Foundation, and the Innovative Research Call in Explosives and Weapons Detection (2007), a cross-government programme sponsored by a number of government departments and agencies under the CONTEST strategy. This research was supported under Australian Research Council's Discovery Projects funding scheme (DP 120 103703).

References

[1] Lee Y-S 2009 *Principles of Terahertz Science and Technology* (Berlin: Springer)
[2] Tonouchi M 2007 Cutting-edge terahertz technology *Nature Photon.* **1** 97–105
[3] Chan W L, Diebel J and Mittleman D M 2007 Imaging with terahertz radiation *Rep. Prog. Phys.* **70** 1325–79
[4] Mittleman D 2003 *Sensing with THz radiation* (Berlin: Springer)
[5] Wallace V P, MacPherson E, Zeitler J A and Reid C 2008 Three-dimensional imaging of optically opaque materials using nonionizing terahertz radiation *J. Opt. Soc. Am.* A **25** 3120–33
[6] Senitzky B and Oliner A A 1970 Submillimeter waves—a transition region *Proc. Symp. on Submillimeter Waves (New York, NY)*
[7] Hartwick T S, Hodges D T, Baker D H and Foote F B 1976 Far infrared imagery *Appl. Opt.* **15** 1919–22
[8] Cheo P K 1978 Far-infrared laser system for detection of defects in polyethylene-insulated power cables *Opt. Lett.* **2** 42–4
[9] Zeitler J A, Shen Y, Baker C, Taday P F, Pepper M and Rades T 2007 Analysis of coating structures and interfaces in solid oral dosage forms by three dimensional terahertz pulsed imaging *J. Pharm. Sci.* **96** 330–40
[10] Yasui T, Yasuda T, Sawanaka K and Araki T 2005 Terahertz paintmeter for noncontact monitoring of thickness and drying progress in paint film *Appl. Opt.* **44** 6849–56
[11] Zeitler J A, Taday P F, Newnham D A, Pepper M, Gordon K C and Rades T 2007 Terahertz pulsed spectroscopy and imaging in the pharmaceutical setting—a review *J. Pharm. Pharmacol.* **59** 209–23
[12] Davies A G, Burnett A D, Fan W, Linfield E H and Cunningham J E 2008 Terahertz spectroscopy of explosives and drugs *Mater. Today* **11** 18–26
[13] Shen Y C, Taday P F, Newnham D A and Pepper M 2005 Chemical mapping using reflection terahertz pulsed imaging *Semicond. Sci. Technol.* **20** S254–7
[14] Fischer B, Hoffmann M, Helm H, Modjesch G and Uhd Jepsen P 2005 Chemical recognition in terahertz time-domain spectroscopy and imaging *Semicond. Sci. Technol.* **20** S246–53
[15] Watanabe Y, Kawase K, Ikari T, Ito H, Ishikawa Y and Minamide H 2003 Component spatial pattern analysis of chemicals using terahertz spectroscopic imaging *Appl. Phys. Lett.* **83** 800–2
[16] Kawase K, Ogawa Y, Watanabe Y and Inoue H 2003 Non-destructive terahertz imaging of illicit drugs using spectral fingerprints *Opt. Express* **11** 2549–54
[17] Lu M, Shen J, Li N, Zhang Y, Zhang C, Liang L and Xu X 2006 Detection and identification of illicit drugs using terahertz imaging *J. Appl. Phys.* **100** 103104
[18] Shen Y C, Lo T, Taday P F, Cole B E, Tribe W R and Kemp M C 2005 Detection and identification of explosives using terahertz pulsed spectroscopic imaging *Appl. Phys. Lett.* **86** 241116
[19] Zelsmann H R 1995 Temperature dependence of the optical constants for liquid H_2O and D_2O in the far IR region *J. Mol. Struct.* **350** 95–114
[20] Wallace V P, Fitzgerlad A J, Shankar S, Flanagan N, Pye R J, Cluff J and Arnone D D 2004 Terahertz pulsed imaging of basal cell carcinoma *ex vivo* and *in vivo Br. J. Dermatol.* **151** 424–32
[21] Fitzgerlad A J, Wallace V P, Jimenez-Linan M, Bobrow L, Pye R J, Purushotham A D and Arnone D D 2006 Terahertz pulsed imaging of human breast tumors *Radiology* **239** 533–40
[22] Hu B B and Nuss M C 1995 Imaging with terahertz waves *Opt. Lett.* **20** 1716–18
[23] Shimosato H, Ashida M, Itoh T, Saito S and Sakai K 2007 *Ultrabroadband Detection of Terahertz Radiation from 0.1 to 100 THz with Photoconductive Antenna* in *Ultrafast Optics V* ed S Watanabe and K Midorikawa (New York: Springer)
[24] Dobroiu A, Yamashita M, Ohshima Y N, Morita Y, Otani C and Kawase K 2004 Terahertz imaging system based on a backward-wave oscillator *Appl. Opt.* **43** 5637–46
[25] Löffler T, May T, am Weg C, Alcin A, Hils B and Roskos H G 2007 Continuous-wave terahertz imaging with a hybrid system *Appl. Phys. Lett.* **90** 091111
[26] Siebert K J, Loffler T, Quast H, Thomson M, Bauer T, Leonhardt R, Czasch S and Roskos H G 2002 All-optoelectronic continuous wave THz imaging for biomedical applications *Phys. Med. Biol.* **47** 3743–8
[27] Gregory I S, Tribe W R, Baker C, Cole B E, Evans M J, Spencer L, Pepper M and Missous M 2005 Continuous-wave terahertz system with a 60 dB dynamic range *Appl. Phys. Lett.* **86** 204104
[28] Kohler R, Tredicucci A, Beltram F, Beere H E, Linfield E H, Davies A G, Ritchie D A, Iotti R C and Rossi F 2002 Terahertz semiconductor-heterostructure laser *Nature* **417** 156–9
[29] Williams B S 2007 Terahertz quantum-cascade lasers *Nature Photon.* **1** 517–25
[30] Scalari G, Walther C, Fischer M, Terazzi R, Beere H E, Ritchie D A and Faist J 2008 THz and sub-THz quantum cascade lasers *Laser Photon. Rev.* **3** 45–66
[31] Chan C W I, Hu Q and Reno J L 2012 Ground state terahertz quantum cascade lasers *Appl. Phys. Lett.* **101** 151108
[32] Fathololoumi S, Dupont E, Chan C W I, Wasilewski Z R, Laframboise S R, Ban D, Mátyás A, Jirauschek C, Hu Q and Liu H C 2012 Terahertz quantum cascade lasers operating up to 200 K with optimized oscillator strength and improved injection tunneling *Opt. Express* **20** 3866–76
[33] Wienold M, Röben B, Schrottke L, Sharma R, Tahraoui A, Biermann K and Grahn H T 2014 High-temperature, continuous-wave operation of terahertz quantum-cascade

lasers with metal–metal waveguides and third-order distributed feedback *Opt. Express* **22** 3334–48
[34] Li L, Chen L, Zhu J, Freeman J, Dean P, Valavanis A, Davies A G and Linfield E H 2014 Terahertz quantum cascade lasers with >1 W output powers *Electron. Lett.* **50** 309–11
[35] Williams B S, Kumar S, Hu Q and Reno J L 2006 High-power terahertz quantum-cascade lasers *Electron. Lett.* **42** 89–90
[36] Vitiello M S, Consolino L, Bartalini S, Taschin A, Tredicucci A, Inguscio M and Natale P D 2012 Quantum-limited frequency fluctuations in a terahertz laser *Nature Photon.* **6** 525
[37] Vitiello M S and Tredicucci A 2011 Tunable emission in THz quantum cascade lasers *IEEE Trans. THz Sci. Technol.* **1** 76–84
[38] Dean P *et al* 2013 Coherent three-dimensional terahertz imaging through self-mixing in a quantum cascade laser *Appl. Phys. Lett.* **103** 181112
[39] Ravaro M, Jagtap V, Santarelli G, Sirtori C, Li L H, Khanna S P, Linfield E H and Barbieri S 2013 Continuous-wave coherent imaging with terahertz quantum cascade lasers using electro-optic harmonic sampling *Appl. Phys. Lett.* **102** 091107
[40] Dean P, Saat N K, Khanna S P, Salih M, Burnett A, Cunningham J, Linfield E H and Davies A G 2009 Dual-frequency imaging using an electrically tunable terahertz quantum cascade laser *Opt. Express* **17** 20631–41
[41] Bründermann E, Havenith M, Scalari G, Giovannini M, Faist J, Kunsch J, Mechold L and Abraham M 2006 Turn-key compact high temperature terahertz quantum cascade lasers: imaging and room temperature detection *Opt. Express* **14** 1829–41
[42] Richter H, Greiner-Bär M, Pavlov S G, Semenov A D, Wienold M, Schrottke L, Giehler M, Hey R, Grahn H T and Hübers H-W 2010 A compact, continuous-wave terahertz source based on a quantum-cascade laser and a miniature cryocooler *Opt. Express* **18** 10177–87
[43] Amanti M I, Scalari G, Beck M and Faist J 2012 Stand-alone system for high-resolution, real-time terahertz imaging *Opt. Express* **20** 2772–8
[44] Darmo J, Tamosiunas V, Fasching G, Kröll J, Unterrainer K, Beck M, Giovannini M, Faist J, Kremser C and Debbage P 2004 Imaging with a terahertz quantum cascade laser *Opt. Express* **12** 1879–84
[45] Chamberlin D R, Robrish P R, Trutna W R, Scalari G, Giovannini M, Ajili L and Faist J 2005 Imaging at 3.4 THz with a quantum cascade-laser *Appl. Opt.* **44** 121–5
[46] Kim S M *et al* 2006 Biomedical terahertz imaging with a quantum cascade laser *Appl. Phys. Lett.* **88** 153903
[47] Ravaro M, Locatelli M, Viti L, Ercolani D, Consolino L, Bartalini S, Sorba L, Vitiello M S and De Natale P 2014 Detection of a 2.8 THz quantum cascade laser with a semiconductor nanowire field-effect transistor coupled to a bow-tie antenna *Appl. Phys. Lett.* **104** 083116
[48] Barbieri S, Alton J, Baker C, Lo T, Beere H E and Ritchie D A 2005 Imaging with THz quantum cascade lasers using a Schottky diode mixer *Opt. Express* **13** 6497–503
[49] Dean P *et al* 2011 Terahertz imaging through self-mixing in a quantum cascade laser *Opt. Lett.* **36** 2587–9
[50] de Cumis U S *et al* 2012 Terahertz confocal microscopy with a quantum cascade laser source *Opt. Express* **20** 21924–31
[51] Williams B S, Kumar S, Callebaut H, Hu Q and Reno J L 2003 Terahertz quantum-cascade laser at $\lambda \approx 100\,\mu$m using metal waveguide for mode confinement *Appl. Phys. Lett.* **83** 2124–6
[52] Adam A J L, Kas alynas I, Hovenier J N, Klaassen T O, Gao J R, Orlova E E, Williams B S, Kumar S, Hu Q and Reno J L 2006 Beam patterns of terahertz quantum cascade lasers with subwavelength cavity dimensions *Appl. Phys. Lett.* **88** 151105
[53] Richter H, Semenov A D, Pavlov S G, Mahler L, Tredicucci A, Beere H E, Ritchie D A, Il'in K S, Siegel M and Hübers H-W 2008 Terahertz heterodyne receiver with quantum cascade laser and hot electron bolometer mixer in a pulse tube cooler *Appl. Phys. Lett.* **93** 141108
[54] Hajenius M *et al* 2008 Surface plasmon quantum cascade lasers as terahertz local oscillators *Opt. Lett.* **33** 312–14
[55] Hübers H W, Pavlov S, Semenov A D, Köhler R, Mahler L, Tredicucci A, Beere H E, Ritchie D A and Linfield E H 2005 Terahertz quantum cascade laser as local oscillator in a heterodyne receiver *Opt. Express* **13** 5890–6
[56] Salih M, Dean P, Valavanis A, Khanna S P, Li L H, Cunningham J E, Davies A G and Linfield E H 2013 Terahertz quantum cascade lasers with thin resonant-phonon depopulation active regions and surface-plasmon waveguides *J. Appl. Phys.* **113** 113110
[57] Orlova E E *et al* 2006 Antenna model for wire lasers *Phys. Rev. Lett.* **96** 173904
[58] Danylov A A, Waldman J, Goyette T M, Gatesman A J, Giles R H, Linden K J, Neal W R, Nixon W E, Wanke M C and Reno J L 2007 Transformation of the multimode terahertz quantum cascade laser beam into a Gaussian, using a hollow dielectric waveguide *Appl. Opt.* **46** 5051–5
[59] Danylov A A *et al* 2010 Terahertz inverse synthetic aperture radar (ISAR) imaging with a quantum cascade laser transmitter *Opt. Express* **18** 16264–72
[60] Nguyen K L *et al* 2006 Three-dimensional imaging with a terahertz quantum cascade laser *Opt. Express* **14** 2123–9
[61] Dean P, Shaukat M U, Khanna S P, Chakraborty S, Lachab M, Burnett A, Davies A G and Linfield E H 2008 Absorption-sensitive diffuse reflection imaging of concealed powders using a terahertz quantum cascade laser *Opt. Express* **16** 5997–6007
[62] Rothbart N, Richter H, Wienold M, Schrottke L, Grahn H T and Hubers H W 2013 Fast 2-D and 3-D terahertz imaging with a quantum-cascade laser and a scanning mirror *IEEE Trans. THz Sci. Technol.* **3** 617–24
[63] Yin X, Ng B W-H, Zeitler J A, Nguyen K L, Gladden L F and Abbott D 2010 Local computed tomography using a THz quantum cascade laser *IEEE Sensors J.* **10** 1718–31
[64] Hoshina H, Sasaki Y, Hayashi A, Otani C and Kawase K 2009 Noninvasive mail inspection system with terahertz radiation *Appl. Spectrosc.* **63** 81–6
[65] Wu Q, Hewitt T D and Zhang X C 1996 Two-dimensional electro-optic imaging of THz beams *Appl. Phys. Lett.* **69** 1026–8
[66] Lee A W M, Williams B S, Kumar S, Hu Q and Reno J L 2006 Real-time imaging using a 4.3-THz quantum cascade laser and a 320×240 microbolometer focal-plane array *IEEE Photon. Technol. Lett.* **18** 1415–17
[67] Lee A W M, Qin Q, Kumar S, Williams B S, Hu Q and Reno J L 2006 Real-time terahertz imaging over a standoff distance (>25 meters) *Appl. Phys. Lett.* **89** 141125
[68] Behnken B N, Karunasiri G, Chamberlin D R, Robrish P R and Faist J 2008 Real-time imaging using a 2.8 THz quantum cascade laser and uncooled infrared microbolometer camera *Opt. Lett.* **33** 440–2
[69] Oda N, Ishi T, Morimoto T, Sudou T, Tabata H, Kawabe S, Fukuda K, Lee A W M and Hu Q 2012 Real-time transmission-type terahertz microscope with palm size terahertz camera and compact quantum cascade laser *Proc. SPIE* **8496** 84960Q
[70] Luo H, Liu H C, Song C Y and Wasilewski Z R 2005 Background-limited terahertz quantum-well photodetector *Appl. Phys. Lett.* **86** 231103
[71] Dean P, Salih M, Khanna S P, Li L H, Saat N K, Valavanis A, Burnett A, Cunningham J E, Davies A G and Linfield E H

2012 Resonant-phonon depopulation terahertz quantum cascade lasers and their application in spectroscopic imaging *Semicond. Sci. Technol.* **27** 094004
[72] Walther C, Fischer M, Scalari G, Terazzi R, Hoyler N and Faist J 2007 Quantum cascade lasers operating from 1.2 to 1.6 THz *Appl. Phys. Lett.* **91** 131122
[73] Kumar S and Hu Q 2009 Coherence of resonant-tunneling transport in terahertz quantum-cascade lasers *Phys. Rev.* B **80** 245316
[74] Kroll J, Darmo J, Dhillon S S, Marcadet X, Calligaro M, Sirtori C and Unterrainer K 2007 Phase-resolved measurements of stimulated emission in a laser *Nature* **449** 698–701
[75] Scalari G, Amanti M I, Walther C, Terazzi R, Beck M and Faist J 2010 Broadband THz lasing from a photon–phonon quantum cascade structure *Opt. Express* **18** 8043–52
[76] Fan J A, Belkin M A, Capasso F, Khanna S P, Lachab M, Davies A G and Linfield E H 2006 Surface emitting terahertz quantum cascade laser with a double-metal waveguide *Opt. Express* **14** 11672–80
[77] Amanti M I, Fischer M, Scalari G, Beck M and Faist J 2009 Low-divergence single-mode terahertz quantum cascade laser *Nature Photon.* **3** 586–90
[78] Mahler L, Tredicucci A, Beltram F, Walther C, Faist J, Beere H E and Ritchie D A 2010 High-power surface emission from terahertz distributed feedback lasers with a dual-slit unit cell *Appl. Phys. Lett.* **96** 191109
[79] Ravaro M, Barbieri S, Santarelli G, Jagtap V, Manquest C, Sirtori C, Khanna S P and Linfield E H 2012 Measurement of the intrinsic linewidth of terahertz quantum cascade lasers using a near-infrared frequency comb *Opt. Express* **20** 25654–61
[80] Barkan A *et al* 2004 Linewidth and tuning characteristics of terahertz quantum cascade lasers *Opt. Lett.* **29** 575–7
[81] Barbieri S, Alton J, Beere H E, Linfield E H, Ritchie D A, Withington S, Scalari G, Ajili L and Faist J 2004 Heterodyne mixing of two far-infrared quantum cascade lasers by use of a point-contact Schottky diode *Opt. Lett.* **29** 1632–4
[82] Rabanus D, Graf U U, Philipp M, Ricken O, Stutzki J, Vowinkel B, Wiedner M C, Walther C, Fischer M and Faist J 2009 Phase locking of a 1.5 Terahertz quantum cascade laser and use as a local oscillator in a heterodyne HEB receiver *Opt. Express* **17** 1159–68
[83] Rothman L S *et al* 2005 The HITRAN 2004 molecular spectroscopic database *J. Quant. Spectrosc. Radiat. Transfer* **96** 139–204
[84] Valavanis A *et al* 2013 Self-mixing interferometry with terahertz quantum cascade lasers *IEEE Sensors J.* **13** 37–43
[85] Walther M, Fischer B M and Uhd Jepsen P 2003 Noncovalent intermolecular forces in polycrystalline and amorphous saccharides in the far infrared *Chem. Phys.* **288** 261–8
[86] Xu J, Hensley J M, Fenner D B, Green R P, Mahler L, Tredicucci A, Allen M G, Beltram F, Beere H E and Ritchie D A 2007 Tunable terahertz quantum cascade lasers with an external cavity *Appl. Phys. Lett.* **91** 121104
[87] Lee A W M, Williams B S, Kumar S, Hu Q and Reno J L 2010 Tunable terahertz quantum cascade lasers with external gratings *Opt. Lett.* **35** 910–12
[88] Mahler L, Tredicucci A, Beltram F, Beere H E and Ritchie D A 2010 Tuning a distributed feedback laser with a coupled microcavity *Opt. Express* **18** 19185–91
[89] Qin Q, Williams B S, Kumar S, Reno J L and Hu Q 2009 Tuning a terahertz wire laser *Nature Photon.* **3** 732–7
[90] Lever L, Hinchcliffe N M, Khanna S P, Dean P, Ikonic Z, Evans C A, Davies A G, Harrison P, Linfield E H and Kelsall R W 2009 Terahertz ambipolar dual-wavelength quantum cascade laser *Opt. Express* **17** 19926–32
[91] Freeman J R, Marshall O P, Beere H E and Ritchie D A 2008 Electrically switchable emission in terahertz quantum cascade lasers *Opt. Express* **16** 19830–5
[92] Khanna S P, Salih M, Dean P, Davies A G and Linfield E H 2009 Electrically tunable terahertz quantum-cascade laser with a heterogeneous active region *Appl. Phys. Lett.* **95** 181101
[93] Chen J, Chen Y, Zhao H, Bastiaans G J and Zhang X C 2007 Absorption coefficients of selected explosives and related compounds in the range of 0.1–2.8 THz *Opt. Express* **15** 12060–7
[94] Liu H-B, Chen Y, Bastiaans G J and Zhang X C 2006 Detection and identification of explosive RDX by THz diffuse reflection spectroscopy *Opt. Express* **14** 415–23
[95] Rakic A D *et al* 2013 Swept-frequency feedback interferometry using terahertz frequency QCLs: a method for imaging and materials analysis *Opt. Express* **21** 22194–205
[96] Tsang L, Kong J A and Shin R T 1985 *Theory of Microwave Remote Sensing* (New York: Wiley)
[97] Lax M 1952 Multiple scattering of waves: II. The effective field in dense systems *Phys. Rev.* **85** 621–9
[98] Dean P, Burnett A D, Tych K, Khanna S P, Lachab M, Cunningham J E, Linfield E H and Davies A G 2011 Measurement and analysis of the diffuse reflectance of powdered samples at terahertz frequencies using a quantum cascade laser *J. Chem. Phys.* **134** 134304
[99] Wertheim M S 1963 Exact solution of the Percus–Yevick integral equation for hard spheres *Phys. Rev. Lett.* **10** 321–3
[100] Barbieri S, Gellie P, Santarelli G, Ding L, Maineult W, Sirtori C, Colombelli R, Beere H and Ritchie D 2010 Phase-locking of a 2.7-THz quantum cascade laser to a mode-locked erbium-doped fibre laser *Nature Photon.* **4** 636–40
[101] Betz A L, Boreiko R T, Williams B S, Kumar S, Hu Q and Reno J L 2005 Frequency and phase-lock control of a 3 THz quantum cascade laser *Opt. Lett.* **30** 1837–9
[102] Danylov A A, Goyette T M, Waldman J, Coulombe M J, Gatesman A J, Giles R H, Goodhue W D, Qian X and Nixon W E 2009 Frequency stabilization of a single mode terahertz quantum cascade laser to the kilohertz level *Opt. Express* **17** 7525–32
[103] Spickermann G, Friederich F, Roskos H G and Bolívar P H 2009 High signal-to-noise-ratio electro-optical terahertz imaging system based on an optical demodulating detector array *Opt. Lett.* **34** 3424–6
[104] Friederich F, Spickermann G, Roggenbuck A, Deninger A, am Weg C, Von Spiegel W, Lison F, Bolivar P H and Roskos H G 2010 Hybrid continuous-wave demodulating multipixel terahertz imaging systems *IEEE Trans. Microwave Theory Tech.* **58** 2022–6
[105] Lang R and Kobayashi K 1980 External optical feedback effects on semiconductor injection laser properties *IEEE J. Quantum Electron.* **QE-16** 347–55
[106] Katz J, Margalit S, Harder C, Wilt D and Yariv A 1981 The intrinsic electrical equivalent circuit of a laser diode *IEEE J. Quantum Electron.* **17** 4–7
[107] Giuliani G, Norgia M, Donati S and Bosch T 2002 Laser diode self-mixing technique for sensing applications *J. Opt. A: Pure Appl. Opt.* **4** S283–94
[108] Green R P, Xu J-H, Mahler L, Tredicucci A, Beltram F, Giuliani G, Beere H E and Ritchie D A 2008 Linewidth enhancement factor of terahertz quantum cascade lasers *Appl. Phys. Lett.* **92** 071106
[109] Lim Y L *et al* 2011 Demonstration of a self-mixing displacement sensor based on terahertz quantum cascade lasers *Appl. Phys. Lett.* **99** 081108
[110] Mezzapesa F P, Columbo L L, Brambilla M, Dabbicco M, Borri S, Vitiello M S, Beere H E, Ritchie D A and

Scamarcio G 2013 Intrinsic stability of quantum cascade lasers against optical feedback *Opt. Express* **21** 13748–57

[111] Mezzapesa F P, Columbo L L, Brambilla M, Dabbicco M, Vitiello M S and Scamarcio G 2014 Imaging of free carriers in semiconductors via optical feedback in terahertz quantum cascade lasers *Appl. Phys. Lett.* **104** 041112

[112] Scalari G, Ajili L, Faist J, Beere H, Linfield E, Ritchie D and Davies G 2003 Far-infrared $\lambda \approx 87\ \mu$m bound-to-continuum quantum-cascade lasers operating up to 90 K *Appl. Phys. Lett.* **82** 3165–7

[113] Indjin D, Harrison P, Kelsall R W and Ikonić Z 2003 Mechanisms of temperature performance degradation in terahertz quantum-cascade lasers *Appl. Phys. Lett.* **82** 1347–9

[114] Lim Y L, Kliese R, Bertling K, Tanimizu K, Jacobs P A and Rakić A D 2010 Self-mixing flow sensor using a monolithic VCSEL array with parallel readout *Opt. Express* **18** 11720–7

[115] Barbieri S, Alton J, Beere H E, Fowler J, Linfield E H and Ritchie D A 2004 2.9 THz quantum cascade lasers operating up to 70 K in continuous wave *Appl. Phys. Lett.* **85** 1674–6

[116] Petermann K 1991 *Laser Diode Modulation and Noise* (Dordrecht: Kluwer)

[117] Jeon T-I and Grischkowsky D 1998 Characterization of optically dense, doped semiconductors by reflection THz time domain spectroscopy *Appl. Phys. Lett.* **72** 3032–4

[118] Jepsen P U, Møller U and Merbold H 2007 Investigation of aqueous alcohol and sugar solutions with reflection terahertz time-domain spectroscopy *Opt. Express* **15** 14717–37

[119] Lui H S *et al* 2014 Terahertz inverse synthetic aperture radar imaging using self-mixing interferometry with a quantum cascade laser *Opt. Lett.* **39** 2629–31

[120] Gunawardena A and Longstaff D 1995 A matched filter based synthetic aperture radar (SAR) algorithm for stepped frequency ground penetrating radar *Record of the IEEE 1995 Int. Radar Conf. (Alexandria, VA)* pp 239–43